

LONGITUDINAL TRACKING OF PULMONARY EPITHELIAL CELL INJURY
AND DETACHMENT DURING SEQUENTIAL RECRUITMENT AND
DERECRUITMENT IN A MODEL OF ATELECTRAUMA

AN ABSTRACT

SUBMITTED ON THE FIFTEENTH DAY OF APRIL 2016

TO THE DEPARTMENT OF BIOMEDICAL ENGINEERING

IN PARTIAL FUFILLMENT OF THE REQUIREMENTS

OF THE SCHOOL OF SCIENCE AND ENGINEERING

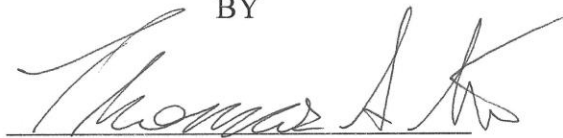
OF TULANE UNIVERSITY

FOR THE DEGREE

OF

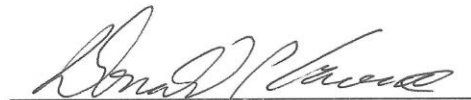
MASTER OF SCIENCE IN ENGINEERING

BY



Thomas A. Itin

Approved:



Donald P. Gaver III, Ph.D.

Chair

Approved:



Walter L. Murfee, Ph.D.

Approved:



Anne-Marie Job, Ph.D.

ABSTRACT

Normal lung mechanics maximize gas exchange across the alveolar-capillary membrane. However, pulmonary diseases such as Acute Respiratory Distress Syndrome (ARDS) disrupt this function by allowing edematous fluid from the vasculature to enter and occlude airways and alveoli. ARDS causes about 59,000 deaths per year in the United States with a mortality rate between 36.2 – 44.3%. To improve gas exchange, patients are often treated with mechanical ventilation, which can cause atelectrauma during the recruitment and derecruitment of occluded airways and alveoli. Previous *in vitro* experiments have modeled the interfacial flow of airway recruitment by introducing a single finger of air into epithelial-lined parallel plate chambers and tubes. The objective of the current study is to longitudinally track the cellular injury and detachment associated with interfacial stresses that arise from 20 cycles of recruitment and derecruitment. We found that cellular injury trends asymptotically from 4.1% after one cycle to 11.2% after 20 cycles. In addition, we found that cellular detachment trends linearly from 0.0 to 6.4% over 20 cycles. The asymptotic behavior of cell damage agrees with conclusions of prior investigations and implies the existence of a ‘critical number’ of bubble passes, above which no additional damage occurs. This cyclic recruitment and derecruitment model provides a platform for investigating the cellular biomechanics leading to epithelial injury during mechanical ventilation of patients with ARDS.

LONGITUDINAL TRACKING OF PULMONARY EPITHELIAL CELL INJURY
AND DETACHMENT DURING SEQUENTIAL RECRUITMENT AND
DERECRUITMENT IN A MODEL OF ATELECTRAUMA

A THESIS

SUBMITTED ON THE FIFTEENTH DAY OF APRIL 2016

TO THE DEPARTMENT OF BIOMEDICAL ENGINEERING

IN PARTIAL FUFILLMENT OF THE REQUIREMENTS

OF THE SCHOOL OF SCIENCE AND ENGINEERING

OF TULANE UNIVERSITY

FOR THE DEGREE

OF

MASTER OF SCIENCE IN ENGINEERING

BY



Thomas A. Itin

Approved:



Donald P. Gaver III, Ph.D.
Chair

Approved:



Walter L. Murfee, Ph.D.

Approved:



Anne-Marie Job, Ph.D.

©Copyright by Thomas A. Itin, 2016
All Rights Reserved

ACKNOWLEDGEMENTS

I would like to thank Dr. Donald Gaver for allowing me to conduct this research under his guidance and mentorship. I also thank my family and friends for their continued support and encouragement through this research process. I extend a special thank you to Sabrina Lynch for motivating me on a daily basis. I thank all the members of the Gaver Lab, especially Michael Harrison and Jeremy Whang, for your tireless efforts and dedication to this body of research. In addition, my success would not have been possible without the generous help from the biomedical engineering department's faculty and staff at Tulane University, especially Mrs. Lorraine McGinley. I would like to thank Mrs. Zartman for encouraging me to consider majoring in engineering rather than business. Finally I would like to thank the Center for Engaged Learning and Teaching as well Newcomb-Tulane College for funding this project and ONY Inc. for their donation of Infasurf pulmonary surfactant.

TABLE OF CONTENTS

ACKNOWLEDGEMENTS.....	II
LIST OF FIGURES	V
LIST OF TABLES.....	X
1. INTRODUCTION	1
2. BACKGROUND.....	3
2.1 LUNG ARCHITECTURE.....	3
2.2 INTERFACIAL MECHANICS.....	5
2.3 PULMONARY SURFACTANT	7
2.4 ACUTE RESPIRATORY DISTRESS SYNDROME.....	9
2.5 VENTILATOR-INDUCED LUNG INJURY.....	11
2.6 FLUID DYNAMICS OF AIRWAY REOPENING	14
2.7 EVIDENCE FOR EPITHELIAL CELL DAMAGE.....	16
2.8 PROJECT RATIONALE	19
2.8.1. <i>Specific Aim 1: Establish a rigid in vitro model of cyclic recruitment and derecruitment using human lung epithelial cells.</i>	20
2.8.2. <i>Specific Aim 2: Quantify the cellular injury associated with an increasing number of recruitment and derecruitment cycles.</i>	20
2.8.3. <i>Specific Aim 3: Track the cellular injury and detachment longitudinally with progressing number of airway recruitment and derecruitment cycles.</i>	20
3. MATERIALS AND METHODS.....	22
3.1 INTRODUCTION	22
3.2 MATERIALS	23
3.2.1 <i>Fibronectin</i>	23
3.2.2 <i>Infasurf</i>	23
3.2.3. <i>Hoechst Stain</i>	24
3.2.4. <i>Ethidium Homodimer-1 Stain</i>	24
3.2.5. <i>Acrylic Syringe Holder</i>	25
3.2.6. <i>Glycerol</i>	26
3.2.7. <i>Experimental Tube Holder</i>	27
3.3 METHODS	28
3.3.1. <i>Epithelial Cell Subculture</i>	28
3.3.2. <i>Tube Pre-treatment</i>	29
3.3.3. <i>Seeding Glass Tubes with Epithelial Cells</i>	30
3.3.4. <i>Media Perfusion</i>	32

3.3.5. <i>Single Recruitment Experimental Protocol</i>	35
3.3.6. <i>Cyclic Recruitment-Derecruitment Experimental Protocol</i>	38
3.3.7. <i>Image Acquisition</i>	40
3.3.8. <i>Longitudinal Cyclic Recruitment-Derecruitment Experimental Protocol</i>	41
3.3.9. <i>Image Analysis</i>	43
3.3.10. <i>Flow Cytometry Data Acquisition</i>	43
3.3.11. <i>Flow Cytometry Analysis</i>	45
3.3.12. <i>Statistical Analysis</i>	46
4. RESULTS	47
4.1 INTRODUCTION	47
4.2 FLOW CYTOMETRY CELL COUNTING	47
4.3 SINGLE SURFACTANT-FREE RECRUITMENT SCENARIO	49
4.4 POPULATION AVERAGE BEHAVIOR OF CYCLIC RECRUITMENT-DERECRUITMENT SCENARIO.....	51
4.5 LONGITUDINAL CYCLIC RECRUITMENT-DERECRUITMENT SCENARIO	52
4.6 MONOLAYER DELAMINATION DUE TO CYCLIC RECRUITMENT-DERECRUITMENT ..	54
5. DISCUSSION	57
5.1 EPITHELIAL CELL DETACHMENT WITH INCREASING NUMBER OF CYCLES	57
5.2 MONOLAYER DELAMINATION BEHAVIOR	59
5.3 EPITHELIAL CELL INJURY WITH SEQUENTIAL RECRUITMENT-DERECRUITMENT EVENTS	62
5.3.1. <i>Surfactant-Free Single Reopening</i>	62
5.3.2. <i>Cyclic Recruitment and Derecruitment with Surfactant-Doped Occlusion Fluid</i>	63
5.4 LIMITATIONS	65
5.5 FUTURE WORK	66
5.5.1. <i>Investigating Mechanisms of Monolayer Delamination</i>	66
5.5.2. <i>Cyclic Recruitment-Derecruitment in Compliant Tubing</i>	67
5.5.3. <i>Cellular Conditioning for Genetic and Cytokine Tests</i>	67
5.5.4. <i>Pulsatile Waveforms during Cyclic Recruitment and Derecruitment</i>	68
5.5.5. <i>Animal Models</i>	68
6. CONCLUSIONS	69
7. APPENDIX	71
7.1 CODE.....	71
REFERENCES	72

LIST OF FIGURES

FIGURE 1.1: CYCLE OF ABNORMAL MECHANICAL STRESSES IMPOSED ON OCCLUDED AIRWAYS DURING A REOPENING EVENT. REOPENING OCCURS BY THE PROPAGATION OF A FINGER OF AIR MOVING FROM LEFT TO RIGHT. CELLS FAR DOWNSTREAM ARE EXPOSED PRIMARILY TO A SHEAR STRESS, AND NEAR THE BUBBLE TIP CELLS EXPERIENCE A LARGE PRESSURE GRADIENT THAT PUSHES THEM OUTWARD DURING AIRWAY REOPENING (GLINDMEYER, 2013).....	2
FIGURE 2.1: LEFT: SCANNING ELECTRON MICROSCOPY IMAGE OF THE 3D STRUCTURE OF ALVEOLI [A] AND ALVEOLAR DUCTS [D]. ALVEOLAR SURFACE AREA CAN BE ESTIMATED DIRECTLY THROUGH QUANTITATIVE MICROSCOPY BY RANDOMLY DROPPING A TEST LINE ON A THIN 2D SECTION (WEIBEL, 2013). RIGHT: DIAGRAMMATIC VISUALIZATION OF THE 23 LUNG GENERATIONS STARTING FROM THE TRACHEA AND ENDING IN THE ALVEOLAR SACKS. ABBREVIATIONS STAND FOR BRONCHI [BR], BRONCHIOLES [BL], TERMINAL BRONCHIOLES [TBL], RESPIRATORY BRONCHIOLES [RBL], ALVEOLAR DUCTS [AD], AND ALVEOLAR SACKS [AS] (WEIBEL, 1963).....	4
FIGURE 2.2: SCHEMATIC DIAGRAM OF PRESSURE – VOLUME LOOPS IN SALINE-FILLED, NORMAL AIR-FILLED AND ACUTE RESPIRATORY DISTRESS SYNDROME LUNGS (GAVER AND GHADIALI, 2008).	6
FIGURE 2.3: PRESSURES REQUIRED TO INFLATE ALVEOLI IN SYSTEMS A) WITHOUT SURFACTANT AND B) WITH SURFACTANT. RED ARROWS REPRESENT HYPOTHETICAL PRESSURE MAGNITUDES, WHICH ARE LARGEST IN THE SMALLEST ALVEOLI FOR THE SYSTEM WITHOUT SURFACTANT.	7
FIGURE 2.4: SURFACTANT INTERFACIAL FILMS DURING COMPRESSION AND EXPANSION OF THE INTERFACE. LEFT: COMPRESSION OF THE INTERFACIAL FILM PRODUCES A SELECTIVE EXCLUSION OF MAINLY UNSATURATED PHOSPHOLIPIDS AND CHOLESTEROL OUT OF THE MONOLAYER TO THE INTERCONNECTED RESERVOIR BY A PROCESS KNOWN AS “SQUEEZE-OUT”. RIGHT: EXPANSION OF THE INTERFACE WITH RE-ADSORPTION OF MATERIAL FROM THE RESERVOIR INTO THE INTERFACIAL MONOLAYER. BOTH PROCESSES ARE FACILITATED BY HYDROPHOBIC SURFACTANT PROTEINS SP-B AND SP-C (LOPEZ-RODRIGUEZ AND PÉREZ-GIL, 2014).	8
FIGURE 2.5: LEFT: NORMAL ALVEOLUS WITH HEALTHY EPITHELIAL CELLS AND AN OPERATIVE SURFACTANT FILM. RIGHT: INJURED ALVEOLUS IN ARDS WITH NECROTIC OR APOPTOTIC TYPE I EPITHELIAL CELLS. ALVEOLAR MACROPHAGES BECOME ACTIVATED, RECRUIT NEUTROPHILS, AND RELEASE INFLAMMATORY CYTOKINES. THE ALVEOLAR-CAPILLARY MEMBRANE INTEGRITY IS COMPROMISED AND SERUM PROTEINS INFILTRATE THE AIRSPACE, COMPETING FOR ADSORPTION AT THE AIR-LIQUID INTERFACE AND INHIBITING SURFACTANT (WARE AND MATTHAY, 2000).	11

FIGURE 2.6: PRESSURE-VOLUME RELATIONSHIP IN AN EXPERIMENTAL MODEL OF ARDS, INDICATING THE ZONES OF VENTILATOR-INDUCED LUNG INJURY AND THE THEORETICAL SAFE ZONE. ARROWS INDICATE THE LOWER AND UPPER INFLECTION POINTS OF THE PRESSURE-VOLUME CURVE (ROTTA AND STEINHORN, 2007).	13
FIGURE 2.7: HYPOTHETICAL STRESSES ON EPITHELIAL CELLS DURING AIRWAY REOPENING IN A) A COLLAPSED COMPLIANT AIRWAY AND B) A FLUID-OCCLUDED RIGID CHANNEL. FOR THE COLLAPSED COMPLIANT AIRWAY, CELLS FAR DOWNSTREAM OF THE BUBBLE EXPERIENCE NOMINAL STRESS. AS THE BUBBLE APPROACHES THE CELL IS PULLED TOWARD THE BUBBLE, AND AS THE BUBBLE PASSES THE CELL IS PUSHED AWAY FROM THE BUBBLE. AFTER THE BUBBLE HAS PASSED, THE CELL EXPERIENCES AN OUTWARD NORMAL STRESS. FOR THE FLUID-OCCLUDED RIGID CHANNEL, CELLS FAR DOWNSTREAM EXPERIENCE A FORWARD TANGENTIAL STRESS. AS THE BUBBLE APPROACHES THE CELL IS PUSHED FORWARD, AND ONCE THE BUBBLE PASSES THE CELL EXPERIENCES AN OUTWARD NORMAL STRESS (BILEK <i>ET AL.</i> , 2003).	14
FIGURE 3.1: FLUORESCENCE SPECTRA OF A) HOECHST 33342 AND B) ETHIDIUM HOMODIMER-1 ACCORDING TO THE MANUFACTURER, THERMOFISHER SCIENTIFIC.	24
FIGURE 3.2: ACRYLIC SYRINGE HOLDER TO TRANSLATE THE MOTION OF THE LINEAR MOTOR TO THE PLUNGER OF THE GAS-TIGHT SYRINGE. A) THE SYRINGE HOLDER ATTACHED TO THE LINEAR MOTOR. B) A VIEW OF THE HOLDER WITH A SYRINGE IN PLACE. C) THE COMPUTER-AIDED DRAWING OF THE SYRINGE HOLDER USED FOR LASER CUTTING.	26
FIGURE 3.3: THE USE OF GLYCEROL FOR OPTICAL COUPLING IS BETTER THAN EITHER AIR OR WATER. A) EXPERIMENTAL TUBE WITH NO COUPLING FLUID. B) EXPERIMENTAL TUBE SUBMERGED IN WATER FOR OPTICAL COUPLING. C) EXPERIMENTAL TUBE SUBMERGED IN GLYCEROL FOR OPTICAL COUPLING.	27
FIGURE 3.4: THE EXPERIMENTAL TUBE HOLDER DESIGNED TO SECURE THE EXPERIMENTAL TUBE WHILE SUBMERGING IT IN GLYCEROL FOR OPTICAL COUPLING. A) A RECTANGULAR CUT IN THE CORD WEATHERSTRIP IS MADE TO SLIDE THE EXPERIMENTAL TUBE INTO THE HOLDER. B) ONCE THE EXPERIMENTAL TUBE IS IN PLACE, THE PLUGS OF CUT WEATHERSTRIP ARE REPLACED AND SMOOTHED OVER WITH SCISSORS TO REMOVE ANY GAPS IN THE WEATHERSTRIP SEAL AGAINST THE TUBE.	28
FIGURE 3.5: EXPERIMENTAL TUBE FOR CELL SEEDING. A) EXPLODED VIEW OF ALL COMPONENTS. LISTED FROM LEFT TO RIGHT THE COMPONENTS ARE: FEMALE BARBED LUER, SILICONE TUBING, BOROSILICATE GLASS TUBE, SILICONE TUBE, AND MALE BARBED LUER. B) ASSEMBLED TUBE.	30
FIGURE 3.6: PERFUSION APPARATUS FOR PERFUSING NEW MEDIA INTO CELL-SEEDED EXPERIMENTAL TUBES. A) SYRINGE PUMP. B) 5mL DISPOSABLE SYRINGE. C) PERFUSION TUBE CONSISTING OF APPROXIMATELY 1 METER OF SILICONE TUBING WITH A MALE OR FEMALE LUER ON EACH END. D) REAR ACCESS PORT TO THE INCUBATOR. E) EXPERIMENTAL TUBE.	33

FIGURE 3.7: HOW TO ASSEMBLE MALE AND FEMALE LUERS WITHOUT INTRODUCING AIR BUBBLES INTO THE SYSTEM. A) BOTH THE MALE AND FEMALE LUERS ARE COMPLETELY FILLED WITH LIQUID SO THAT A MENISCUS EXTENDS PAST THE LUER OPENING. B) THE LUERS ARE SLOWLY MOVED TOWARD EACH OTHER SO THAT THE TWO MENISCI JOIN TOGETHER. C) THE LUERS ARE LOCKED TIGHTLY TOGETHER TO COMPLETE THE ASSEMBLY.....	34
FIGURE 3.8: MOVEMENT OF FLUIDS AT DIFFERENT TIME POINTS DURING THE SINGLE RECRUITMENT EXPERIMENT. A) THE OCCLUSION FLUID FILLS THE EXPERIMENTAL TUBE SEEDED WITH CELLS. B) AIR FROM THE UPSTREAM TUBE IS DISPLACED FORWARD BY THE SYRINGE PUMP, CREATING A RECRUITMENT EVENT. C) THE UPSTREAM TUBE IS EXCHANGED FOR TUBE FILLED WITH STAINING SOLUTION. D) THE STAINING SOLUTION FROM THE UPSTREAM TUBE IS DISPLACED FORWARD BY THE SYRINGE PUMP, CREATING A DERECRUITMENT EVENT. THE STAINING SOLUTION CONTAINS PULMONARY SURFACTANT TO REDUCE THE CELLULAR DAMAGE ASSOCIATED WITH THIS MANDATORY DERECRUITMENT.	37
FIGURE 3.9: THE WAVEFORM GENERATED TO RUN THE LINEAR MOTOR DURING CYCLIC EXPERIMENTS. LEFT: THE WAVEFORM PROGRAMMED DIRECTLY INTO THE LINEAR MOTOR. RIGHT: THE EXPECTED WAVEFORM IN THE EXPERIMENTAL TUBE AFTER ADJUSTING FOR THE DIAMETER CHANGE BETWEEN THE GAS-TIGHT SYRINGE AND THE EXPERIMENTAL TUBE. THE RESULT IS A BUBBLE TIP VELOCITY OF 25MM/S IN THE EXPERIMENTAL TUBE.....	40
FIGURE 3.10: SCATTER PLOT OF THE FLOW CYTOMETRY DATA FROM A REPRESENTATIVE SAMPLE. FORWARD SCATTER (FSC) IS PLOTTED VERSUS SIDE SCATTER (SSC), AND EVENTS WITH BOTH LOW FSC AND LOW SSC INTENSITIES WERE GATED OUT AND CLASSIFIED AS DEBRIS. THE REMAINING EVENTS WERE CLASSIFIED AS CELLS AND REPORTED BY TOTAL COUNT.....	46
FIGURE 4.1: CROSS SECTION OF AN EXPERIMENTAL TUBE SHOWING APPROXIMATE SURFACE AREA COVERED WITH A HIGH CONFLUENCE MONOLAYER.	48
FIGURE 4.2: GRAPH COMPARING THE PERCENT OF CELL DEATH FOR VARYING RECRUITMENT VELOCITIES FOR A SINGLE SURFACTANT-FREE RECRUITMENT SCENARIO. THE STAINING SOLUTION WAS INTRODUCED INTO THE RECRUITED TUBE USING PULMONARY SURFACTANT AND A FAST DERECRUITMENT VELOCITY TO MINIMIZE DAMAGE. A ONE-WAY ANOVA TEST WAS CONDUCTED FOR SIGNIFICANCE WITH A TUKEY POST-TEST (**p < 0.01; ***p < 0.001). DISPLAYED ARE GROUP MEANS WITH STANDARD ERROR OF THE MEAN BARS FOR N = 5 TRIALS PER GROUP (CONTROL = $2.1 \pm 1.1\%$; SLOW = $9.4 \pm 1.9\%$; FAST = $5.7 \pm 1.3\%$).....	49
FIGURE 4.3: FIGURE SHOWING A REPRESENTATIVE IMAGE EXAMPLE FOR EACH EXPERIMENTAL GROUP. GRAYSCALE IMAGES WERE ACQUIRED SEPARATELY FOR EACH STAIN, COUNTED, FALSELY COLORED, AND COMBINED INTO A COLORED COMPOSITE. ETHIDIUM HOMODIMER-1 STAINS THE DNA OF CELLS WITH A PERMEABILIZED MEMBRANE (DEAD CELLS) WHILE HOECHST STAINS THE DNA OF ALL CELLS.	50

FIGURE 4.4: GRAPH COMPARING THE PERCENT OF CELL DEATH FOR VARYING NUMBER OF FAST (25 MM/S) RECRUITMENT-DERECRUITMENT CYCLES. THE STAINING SOLUTION WITH 1.0 MG/ML PULMONARY SURFACTANT WAS USED AS THE OCCLUSION FLUID. THE SOLUTION WAS DISPLACED FORWARD DURING RECRUITMENT WITH AN AIR BUBBLE AND RETRACTED BACK INTO THE EXPERIMENTAL TUBE DURING DERECRUITMENT. A ONE-WAY ANOVA TEST WAS CONDUCTED FOR SIGNIFICANCE WITH A TUKEY POST-TEST (*P < 0.05; ***P < 0.001). DISPLAYED ARE GROUP MEANS WITH STANDARD ERROR OF THE MEAN BARS FOR N = 5 TRIALS PER GROUP (CONTROL = $1.5 \pm 0.79\%$; 1 CYCLE = $4.0 \pm 1.4\%$; 10 CYCLES = $10 \pm 1.7\%$).	51
FIGURE 4.5: GRAPH OF THE PERCENT OF CELL DEATH, PERCENT OF CELL DETACHMENT, AND COMBINED PERCENT OF CELL DEATH AND DETACHMENT AT 1, 5, 10, 15, AND 20 CYCLES DURING THE LONGITUDINAL CYCLIC RECRUITMENT-DERECRUITMENT SCENARIO WITH N = 5 TUBES. THE STAINING SOLUTION WITH SURFACTANT WAS DISPLACED FORWARD DURING RECRUITMENT WITH AN AIR BUBBLE AND RETRACTED BACK INTO THE EXPERIMENTAL TUBE DURING DERECRUITMENT AT A FAST VELOCITY OF 25 MM/S. DISPLAYED ARE MEANS WITH STANDARD ERROR OF THE MEAN BARS.	53
FIGURE 4.6: GRAPH OF CELL POPULATIONS AT 1, 5, 10, 15, AND 20 CYCLES DURING THE LONGITUDINAL CYCLIC RECRUITMENT-DERECRUITMENT SCENARIO WITH N = 5 TUBES. THE STAINING SOLUTION WITH SURFACTANT WAS DISPLACED FORWARD DURING RECRUITMENT WITH AN AIR BUBBLE AND RETRACTED BACK INTO THE EXPERIMENTAL TUBE DURING DERECRUITMENT AT A FAST VELOCITY OF 25 MM/S. THE MEANS OF N = 5 TUBES ARE DISPLAYED.	53
FIGURE 4.7: SCHEMATIC SHOWING ‘MONOLAYER DELAMINATION.’	54
FIGURE 4.8: SCHEMATIC SHOWING THE DIRECTIONALITY OF RECRUITMENT AND DERECRUITMENT RELATIVE TO POSITIONS 0-5 USED FOR ACQUIRING MICROGRAPHS. THE EXACT SAME LOCATION WAS IMAGED AFTER EACH SET OF RECRUITMENT-DERECRUITMENT CYCLES, MADE POSSIBLE BY A COMPUTERIZED X-Y-Z STAGE CONTROLLER.....	55
FIGURE 4.9: MICROGRAPHS FROM ALL 6 POSITIONS OF TWO REPRESENTATIVE EXAMPLES TUBES SHOWING ‘MONOLAYER DELAMINATION.’	56
FIGURE 5.1: TOP: PREVIOUS MODEL BY KAY <i>ET AL.</i> (2004). DEMONSTRATION OF SUBSTRATE DENUDATION FROM CYCLIC RECRUITMENT AND DERECRUITMENT WITH L2 CELLS AT A VELOCITY OF 40 MM/S. CELLS WERE FIXED WITH FORMALINE AND STAINED WITH COOMASSIE BRILLIANT BLUE. BOTTOM: CURRENT STUDY DEMONSTRATING MINIMAL CELL DETACHMENT (ABOUT 6.4%) WITH H441 CELLS AT A VELOCITY 27 MM/S. CELLS WERE STAINED WITH HOECHST AND IMAGED USING FLUORESCENCE MICROSCOPY. ...	59
FIGURE 5.2: POSSIBLE MODES OF STRESS FAILURE RESULTING IN THE OBSERVED ‘MONOLAYER DELAMINATION,’ INCLUDING APICAL PEELING DUE TO PRESSURE GRADIENT AND BASOLATERAL BUCKLING DUE TO TRANSMITTED STRESSES. ONCE THE CELL LAYER DETACHES, THE STRESS FIELD WILL	

BE MODIFIED FROM THE IDEAL SIMULATION PREDICTIONS PROVIDED BY PREVIOUS COMPUTATIONAL MODELS.....	61
FIGURE 5.3: PREVIOUS COMPUTATIONAL RESULTS FOR MECHANICAL STRESSES DURING AIRWAY RECRUITMENT. LEFT: SHEAR STRESS AND PRESSURE GRADIENT ON APICAL MEMBRANE (BILEK <i>ET AL.</i> , 2003). RIGHT: NORMAL AND TANGENTIAL STRESSES TRANSMITTED TO BASOLATERAL MEMBRANE (JACOB AND GAVER, 2012).	61
FIGURE 5.4: COMPARISON OF CELL DEATH FOR MULTIPLE RECRUITMENT AND DERECUITMENT CYCLES IN TWO MODELS. TOP: THE EFFECT OF REPEATED BUBBLE PASSES ON ATTACHED CELL DEATH IN AN EXPERIMENT BY YALCIN <i>ET AL.</i> (2007). NOTE THE ‘CRITICAL NUMBER’ OF BUBBLE PASSAGES IS APPROXIMATELY 3. BOTTOM: THE EFFECT OF REPEATED BUBBLE PASSES ON CELL DETACHMENT, DEATH, AND COMBINED DEATH + DETACHMENT IN THE CURRENT STUDY. FOR A MORE ACCURATE COMPARISON, THE PERCENT CELL DEATH RELATIVE TO THE NUMBER OF ATTACHED CELLS WAS CALCULATED AND REPRESENTED WITH A BLACK LINE.....	64

LIST OF TABLES

TABLE 2.1: A BRIEF SUMMARY OF METHODS AND CONCLUSIONS FROM RELEVANT <i>IN VITRO</i> EXPERIMENTS ON AIRWAY REOPENING.	17
TABLE 3.1: APPROXIMATE REFRACTIVE INDICES FOR MATERIALS USED IN EXPERIMENTAL SETUP DURING FLUORESCENCE MICROSCOPY.	27
TABLE 4.1: STATISTICS FOR ALL GROUPS OF $N = 5$ TRIALS IN THE LONGITUDINAL CYCLIC RECRUITMENT AND DERECRUITMENT SCENARIO, REPRESENTED BY $\text{MEAN} \pm \text{STANDARD DEVIATION}$	54

1. INTRODUCTION

The lung is a complex bifurcating network of airways designed to maximize gas transport across the alveolar-capillary membrane. By lining the epithelium along airways, a thin layer of liquid creates an air-liquid interface, and the surface tension of this interface affects overall lung mechanics. Type II airway epithelial cells naturally secrete a protective protein-lipid complex called surfactant into the lining fluid to lower surface tension, modulate surface tension during breathing, and equilibrate pressures between alveoli of differing sizes. These interfacial dynamics can be drastically affected by pulmonary disease.

During Acute Respiratory Distress Syndrome (ARDS), epithelial cell injury leads to permeability of the alveolar-capillary membrane. As a result protein-rich edematous fluid enters the airways, deactivating surfactant by competitive adsorption and leading to neutrophil-derived inflammation. Pulmonary edema leads to impaired gas exchange across fluid-occluded and collapsed airways. To improve oxygenation, patients are treated with mechanical ventilation that can lead to ventilator-induced lung injury (VILI) through two distinct biophysical mechanisms: volutrauma and atelectrauma. Volutrauma is the damage of small airways and alveoli by tissue stretch due to excessive tidal volumes, while atelectrauma is the injury resulting from cyclic opening and closing (recruitment and derecruitment) of small airways and alveoli due to inadequately low tidal volumes.

Occluded airway reopening has been shown to cause cellular injury *in vitro* due to a complex cycle of mechanical stresses that results from the interfacial flow of a progressing air bubble (**Figure 1.1**). Previous studies have demonstrated that cellular injury is most clearly associated with a large pressure gradient at the tip of the progressing bubble. While previous studies in parallel plate chambers have contributed greatly to our understanding of airway reopening, they lack the physiologically relevant characteristics of cylindrical geometry, pulmonary surfactant, and cyclic interfacial flow. In addition, the trends in cellular injury and detachment with multiple cycles of airway recruitment and derecruitment have been poorly defined. This study aims to quantify the magnitude of cellular injury and detachment associated with interfacial stresses arising from the cyclic progression and retraction of an air-liquid interface using an *in vitro* airway occlusion model.

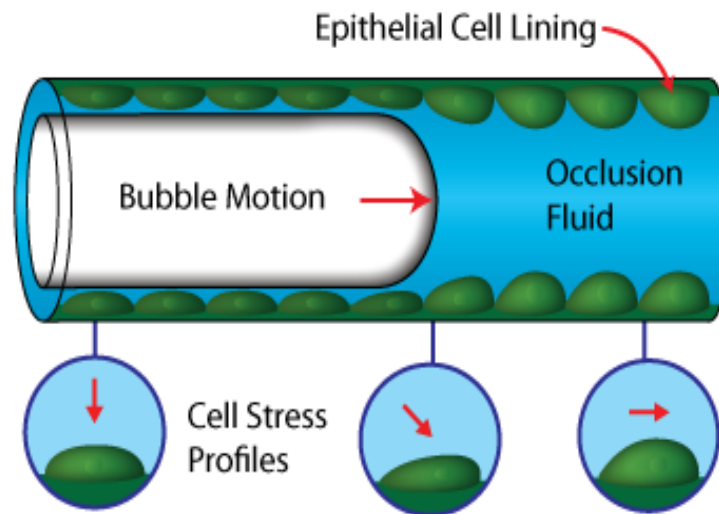


Figure 1.1: Cycle of abnormal mechanical stresses imposed on occluded airways during a reopening event. Reopening occurs by the propagation of a finger of air moving from left to right. Cells far downstream are exposed primarily to a shear stress, and near the bubble tip cells experience a large pressure gradient that pushes them outward during airway reopening (Glindmeyer, 2013).

2. BACKGROUND

2.1 Lung Architecture

The lung is a complex network of bifurcating airways beginning with a single trachea and terminating in approximately 300×10^6 alveoli (Weibel, 1962). The lung structure maximizes surface area for gas exchange along the alveolar-capillary membrane. Air from the external environment enters through the trachea and reaches the first bifurcation (generation) at the carina of the trachea, where the airway bifurcates into the two primary bronchi. The primary bronchi continue to bifurcate into the bronchioles, respiratory bronchioles, alveolar ducts, and alveolar sacs. The conducting airways of the lung correspond to the first 16 generations and are primarily responsible for providing a low resistance pathway to the respiratory zone. The conducting airways also aid in conditioning inhaled air to be warm, humidified, and cleared of foreign particles before reaching the respiratory zone. Generations 17-23 correspond to the respiratory zone, which consists of respiratory bronchioles, alveolar ducts, and alveolar sacs. The walls of airways in the respiratory zone are much more compliant and thin than in the conducting zone. To appreciate the complex and diverse nature of this respiratory zone, it is important to visualize the lung parenchyma (tissue involved in gas transport) in three dimensions as shown in **Figure 2.1**.

The primary function of the respiratory zone is to provide sites for gas transport across the alveolar-capillary membrane, where the respiratory system meets the cardiovascular system. The alveolar-capillary membrane consists of two barriers, the

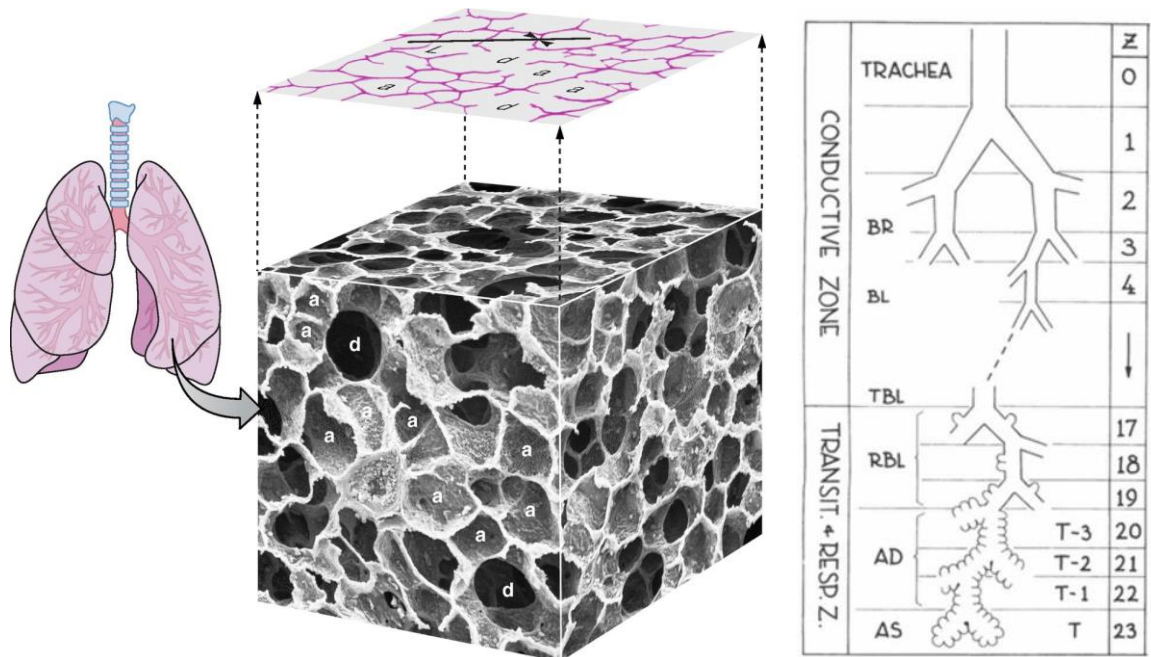


Figure 2.1: Left: Scanning electron microscopy image of the 3D structure of alveoli [a] and alveolar ducts [d]. Alveolar surface area can be estimated directly through quantitative microscopy by randomly dropping a test line on a thin 2D section (Weibel, 2013). Right: Diagrammatic visualization of the 23 lung generations starting from the trachea and ending in the alveolar sacs. Abbreviations stand for bronchi [BR], bronchioles [BL], terminal bronchioles [TBL], respiratory bronchioles [RBL], alveolar ducts [AD], and alveolar sacs [AS] (Weibel, 1963).

alveolar epithelium and the capillary endothelium, with interstitial fluid in between. The alveolar epithelium is composed of a single layer of epithelial cells with two distinct cell types. Type I epithelial cells have a flattened morphology and cover approximately 90% of the epithelium surface area, while type II epithelial cells have a cuboidal morphology and cover approximately 10% of the surface area. Type I epithelial cells are responsible for creating a tight impermeable barrier between the alveolar air space and the interstitial fluid, although this barrier can be compromised during pathologies such as Acute Respiratory Distress Syndrome. Type II epithelial cells provide a transport mechanism for removal of edema fluid from the alveolar air space and secrete pulmonary surfactant that adsorbs to the surface of the alveolar liquid lining. The alveoli are enveloped by extensive capillary beds, which bring erythrocytes in the blood close to the alveoli for

exchange of carbon dioxide for oxygen. Because the distance between the gas in the alveoli and the blood in the capillaries is so thin, diffusion is sufficient for gas transport across the alveolar-capillary membrane. After oxygenation in the pulmonary capillaries, blood returns to the left atrium of the heart through the pulmonary veins and is subsequently pumped through the cardiovascular system.

2.2 Interfacial Mechanics

A thin layer of liquid lines the airways and alveoli of the lung. Surface tension at the air-liquid interface of this liquid coating results from an imbalance of attractive interactions between molecules directly in contact with the gas phase, resulting in a net tendency to minimize surface area. The surface tension can therefore be considered the energy per unit area needed to overcome the forces that minimize exposed area (Lopez-Rodriguez and Pérez-Gil, 2014). The surface tension of the alveolar lining fluid impacts the overall mechanics of lung inflation, and patients with diseased lungs can experience difficulty breathing due to insufficient modulation of surface tension by deficient pulmonary surfactant.

Figure 2.2 shows a schematic diagram of pressure-volume (P-V) loops for normal air-filled lungs compared to saline-filled and diseased lungs. Several observations can be made. First, the pressures necessary to inflate an air-filled lung are much higher than those required to inflate a fluid-filled lung. Lungs of patients with Acute Respiratory Distress Syndrome require even greater pressures to inflate due to surfactant dysfunction. In addition, the slope of the P-V loop for a fluid-filled lung is greater, suggesting a higher degree of lung compliance. This indicates that interfacial forces oppose lung inflation and that normal lung function incorporates a mechanism to lower these surface tension forces.

Finally, the hysteresis difference between inflation and deflation curves demonstrates that the surface tension is modulated during different phases of the respiratory cycle. The natural function of lowering and modifying surface tension in the lung can be attributed to pulmonary surfactant.

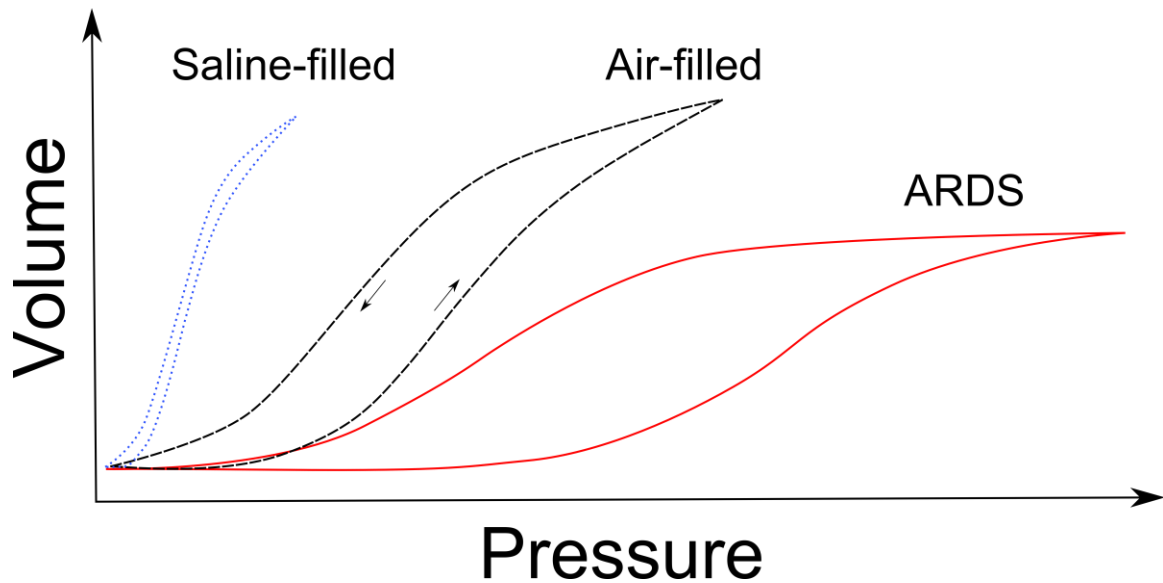


Figure 2.2: Schematic diagram of pressure – volume loops in saline-filled, normal air-filled and Acute Respiratory Distress Syndrome lungs (Gaver and Ghadiali, 2008).

When considering two nearly-spherical alveoli of different radii, the need for a surface tension modulating mechanism is evident. The Law of Laplace establishes that two interconnected alveoli with different radii and the same surface tension cannot coexist at a given pressure (Lopez-Rodriguez and Pérez-Gil, 2014). Laplace's equation states $\Delta P = \frac{2\gamma}{R}$, where P is the closing pressure of a spherical chamber, γ is the surface tension, and R is the radius.

According to the Law of Laplace, if two interconnected alveoli existed with different radii, the pressure difference between the alveoli would cause air to flow from the smaller alveolus into the larger one (**Figure 2.3**). This would result in the collapse of the smaller alveolus. For this reason, pulmonary surfactant plays a major role in

stabilizing the lungs by decreasing the surface tension as a function of alveolar size so that there is no net flow between alveoli (**Figure 2.3**).

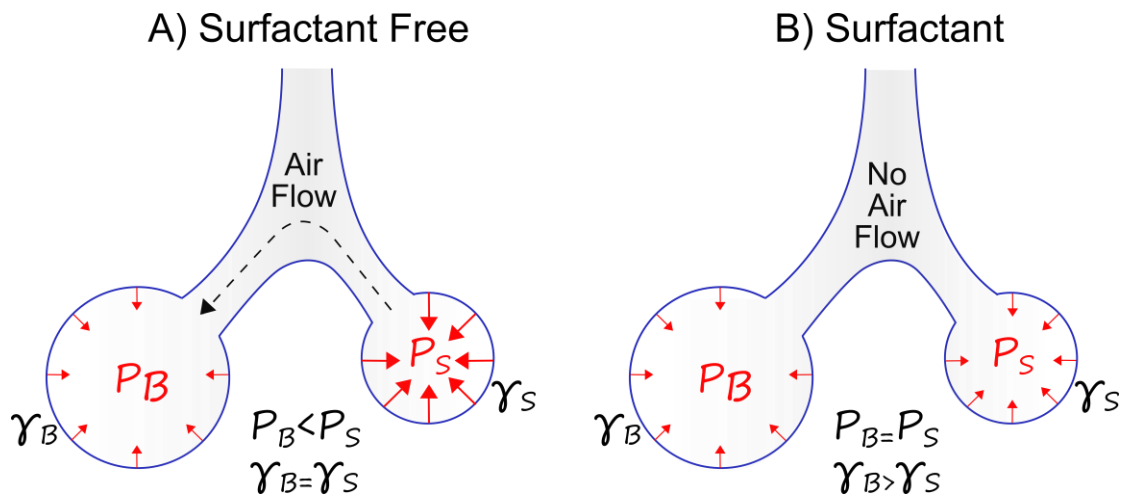


Figure 2.3: Pressures required to inflate alveoli in systems A) without surfactant and B) with surfactant. Red arrows represent hypothetical pressure magnitudes, which are largest in the smallest alveoli for the system without surfactant.

2.3 Pulmonary Surfactant

Pulmonary surfactant plays an essential role in lowering surface tension at the alveolar air-liquid interface, which optimizes the mechanics of breathing and prevents alveolar collapse. Pulmonary surfactant is composed of about 90% lipids and 10% proteins by mass. In humans the most abundant lipid species is dipalmitoylphosphatidylcholine (DPPC), which provides an extreme reduction in surface tension with its surface active function of replacing interfacial water molecules. Due to the saturated nature of DPPC, it is the only component of pulmonary surfactant that can be condensed upon compression of the interfacial monolayer at physiological temperatures, forming a highly lateral packed state (Wüstneck *et al*, 2005). The protein fraction of surfactant, approximately 10% by mass, includes four specific surfactant proteins that can be classified into two families: SP-A and SP-D are hydrophilic while SP-B and SP-C are hydrophobic. SP-A is the most abundant surfactant protein and participates with SP-D in

pulmonary host defense by clearing a variety of bacterial, fungal, and viral pathogens (Parra and Pérez-Gil, 2015; Han and Mallampalli, 2015; Orgeig *et al*, 2010). SP-B and SP-C on the other hand are necessary to promote efficient interfacial adsorption, film stability, and re-spreading abilities of surfactant during continuous compression-expansion breathing cycles.

As we breathe, surfactant interfacial films are subjected to cyclic compression and expansion. To stabilize alveoli, surfactant tightly packs the interfacial film during compression, and subsequently re-adsorbs to the interface during expansion (**Figure 2.4**). The lateral compaction of the interfacial film during inhalation is optimized by the “squeeze out” process where less stable unsaturated phospholipids and neutral lipids are excluded to multi-layered complexes, leaving behind an interfacial film enriched in DPPC (Pérez-Gil and Weaver, 2010). The re-extension of the interfacial film during inhalation involves adsorption of protein-lipid complexes from interconnected reservoirs back onto the interface. Fully functional surfactant films exhibit reduced hysteresis and area compression (<20%) while reaching minimum surface tension (Lopez-Rodriguez and Pérez-Gil, 2014).

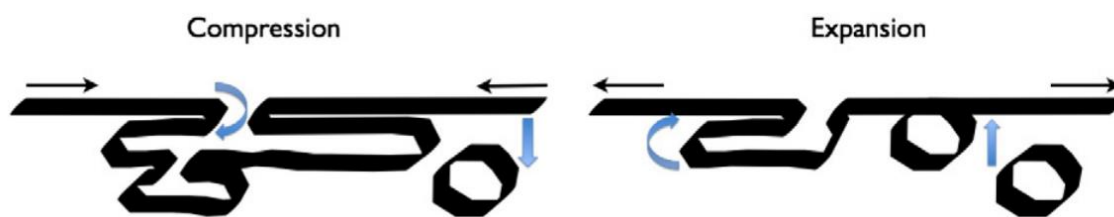


Figure 2.4: Surfactant interfacial films during compression and expansion of the interface. Left: compression of the interfacial film produces a selective exclusion of mainly unsaturated phospholipids and cholesterol out of the monolayer to the interconnected reservoir by a process known as “squeeze-out”. Right: expansion of the interface with re-adsorption of material from the reservoir into the interfacial monolayer. Both processes are facilitated by hydrophobic surfactant proteins SP-B and SP-C (Lopez-Rodriguez and Pérez-Gil, 2014).

2.4 Acute Respiratory Distress Syndrome

Acute Respiratory Distress Syndrome (ARDS), the more severe form of Acute Lung Injury (ALI), is a respiratory pathology characterized by diffuse alveolar damage, alveolar-capillary membrane leakage, and protein rich pulmonary edema (Dushianthan *et al.*, 2011). ARDS has an estimated incidence of 141,500 new cases per year in the United States with an annual death rate of 59,000 per year (Rubenfeld *et al.*, 2005). Pooled mortality rates suggest that the mortality for ARDS is between 36.2% for randomized controlled studies and 44.3% for observational studies (Phua *et al.*, 2009). The pathogenesis for Acute Respiratory Distress Syndrome consists of two pathways: direct effects from lung cell insults such as pneumonia or aspiration of gastric contents and indirect effects from a systemic inflammatory response like sepsis (Bernard *et al.*, 1994). Pre-existing conditions that may increase a patient's risk of developing ARDS include chronic lung disease, chronic alcoholism, or being over the age of 65 (Mokra and Kosutova, 2015). It should be noted that pathological progression of ARDS is rapid, with most patients developing diffuse alveolar infiltrates and progressing to respiratory failure within 48 hours of the onset of symptoms (Mortelliti and Manning, 2002).

Before 1994, there was little consensus on the clinical definition of Acute Lung Injury and Acute Respiratory Distress Syndrome. It was decided that ALI can be applied to a wide spectrum of pathologies while ARDS should be reserved for only the most severe end of the ALI spectrum (Bernard *et al.*, 1994). In 1994 the American-European Consensus Conference proposed three diagnostic criteria for ARDS. The first criterion is the presence of acute severe hypoxemia, defined as a ratio of arterial oxygen tension over fractional inspired oxygen ($\text{PaO}_2/\text{FiO}_2$) less than 200 mm Hg. If this ratio is between

200 mm Hg and 300 mm Hg, the criteria for ALI are met. The second and third criteria for ARDS are bilateral infiltrates on chest radiography and the absence of raised pulmonary artery wedge pressure. This American-European Consensus Conference definition is now widely accepted as a diagnostic tool for ARDS.

The pathological consequences of ARDS are epithelial injury, lung edema, neutrophil-derived inflammation, and surfactant dysfunction as illustrated in **Figure 2.5** (Mokra and Kosutova, 2015). Damage to type I epithelial cells during ARDS compromises the alveolar-capillary membrane, allowing edema fluid to infiltrate the alveolar space. This leakage of serum proteins such as albumin, hemoglobin, and fibrinogen can inhibit surfactant by competing for adsorption to the air-liquid interface (Parra and Pérez-Gil, 2015). Surfactant dysfunction is evident in bronchial lavages recovered from ARDS patients, where changes in phospholipid composition and decreased levels of surfactant proteins have been observed (Dushianthan *et al.*, 2011).

The use of exogenous surfactants in surfactant replacement therapy has been proposed for treatment of surfactant inhibition and dysfunction, but clinical trials have shown limited efficacy (Parra and Pérez-Gil, 2015). Meanwhile, damage to type II epithelial cells impairs surfactant synthesis and metabolism, leading to increased alveolar surface tension and alveolar collapse (Dushianthan *et al.*, 2011). Type II cell injury can also disrupt normal epithelial fluid transport, impairing the removal of edema fluid and prolonging the negative effects of serum protein leakage (Ware and Matthay, 2000).

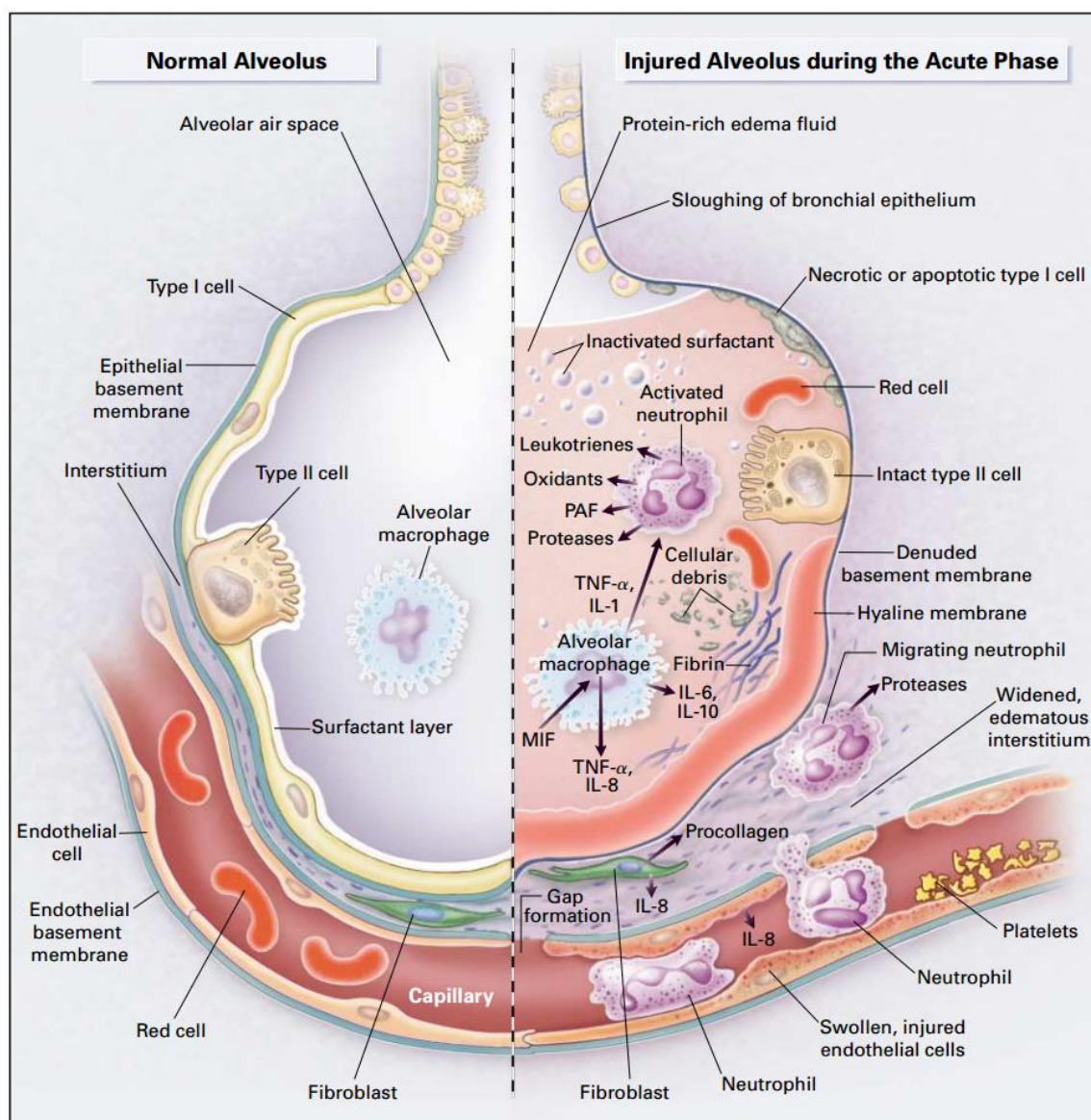


Figure 2.5: Left: Normal alveolus with healthy epithelial cells and an operative surfactant film. Right: Injured alveolus in ARDS with necrotic or apoptotic type I epithelial cells. Alveolar macrophages become activated, recruit neutrophils, and release inflammatory cytokines. The alveolar-capillary membrane integrity is compromised and serum proteins infiltrate the airspace, competing for adsorption at the air-liquid interface and inhibiting surfactant (Ware and Matthay, 2000).

2.5 Ventilator-Induced Lung Injury

The primary goal of mechanical ventilation is to improve gas exchange while minimizing the work of breathing. Mechanical ventilation was previously conceived of as a harmless support modality employed to keep patients alive while the underlying

pathology was treated. It is now recognized that mechanical ventilation can lead to ventilator-induced lung injury (VILI) through two distinct biophysical mechanisms: volutrauma and atelectrauma (Seah *et al.*, 2011).

Volutrauma is the damage to small airways and alveoli by tissue stretch. It has been demonstrated that excessive tidal volume, not airway pressure, is the cause of injury by regional overdistension (Rotta and Steinhorn, 2007). Because patients with ARDS have relatively non-aerated dependent lung regions (regions that are lower with respect to gravity and are more likely to be collapsed) and relatively normally aerated non-dependent lung regions, there is a smaller volume available for ventilation (Slutsky and Ranieri, 2013). Conventional mechanical ventilation employs relatively high tidal volumes of 12 to 15 mL per kilogram of body weight compared to normal tidal volumes of 6 to 7 mL per kilogram (Ware and Matthay, 2000). In a clinical trial enrolling 861 patients with ALI and ARDS, the Acute Respiratory Distress Syndrome Network compared a conventional tidal volume of 12 ml per kilogram with a lower tidal volume of 6 ml per kilogram, finding that mortality was reduced by 22 percent (from 39.8% to 31%) in the group treated with lower tidal volumes (2000). This finding indicates that ventilator management must achieve a balance between providing gas exchange that sustains life and minimizing ventilator-induced lung injury.

Simply ventilating at low tidal volumes is not adequate, because low-volume ventilation can lead to cyclic opening and closing (recruitment and derecruitment) of small airways and alveoli (see **section 2.6** on fluid dynamics of airway reopening), causing lung injury independent of overdistention (**Figure 2.6**). The injury resulting from

recruitment and derecruitment of airways and alveoli is termed atelectrauma and is characterized by epithelial sloughing, hyaline membranes, and pulmonary edema.

Conventionally it has been thought that the atelectrauma is caused by the shear stress associated with alveolar and airway re-opening, but recent studies have shown that the pressure gradient is the primary determinant of mechanical damage to epithelium (Bilek *et al.*, 2003; Kay *et al.*, 2004; Jacob and Gaver, 2012; Glindmeyer *et al.*, 2012; Harrison, 2015). The application of adequate positive end-expiratory pressure (PEEP) has been suggested as method of reducing atelectrauma (Rotta and Steinhorn, 2007). By reducing tidal volumes to avoid volutrauma and maintaining adequate PEEP to prevent atelectrauma, a theoretical safe zone for mechanical ventilation of patients with ARDS can be established (**Figure 2.6**).

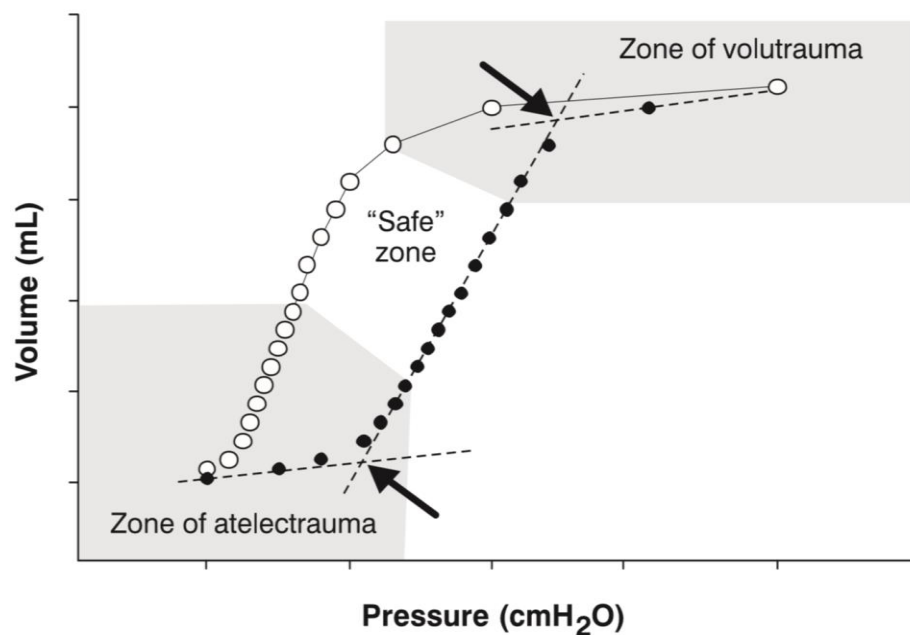


Figure 2.6: Pressure-volume relationship in an experimental model of ARDS, indicating the zones of ventilator-induced lung injury and the theoretical safe zone. Arrows indicate the lower and upper inflection points of the pressure-volume curve (Rotta and Steinhorn, 2007).

2.6 Fluid Dynamics of Airway Reopening

To understand the mechanisms responsible for airway epithelial cell injury during recruitment and derecruitment of fluid-filled airways, it is necessary to analyze the fluid dynamics of airway reopening. The reopening of an occluded airway in an edematous lung can be modeled as the interfacial propagation of a semi-infinite air bubble down a fluid-filled chamber. Computational studies suggest that the mechanical stresses associated with airway reopening include tangential shear stresses, normal stresses, and the spatial and temporal gradients of either of these stresses (Gaver *et al.*, 1996; Bilek *et al.*, 2003). The hypothetical stresses for a collapsed compliant airway and a fluid-occluded rigid channel are shown in **Figure 2.7**. These mechanical stresses can directly damage the epithelial cell by either rupturing the plasma membrane or disrupting cell-to-cell and cell-to-substrate adhesions. In addition epithelial cells can be indirectly affected

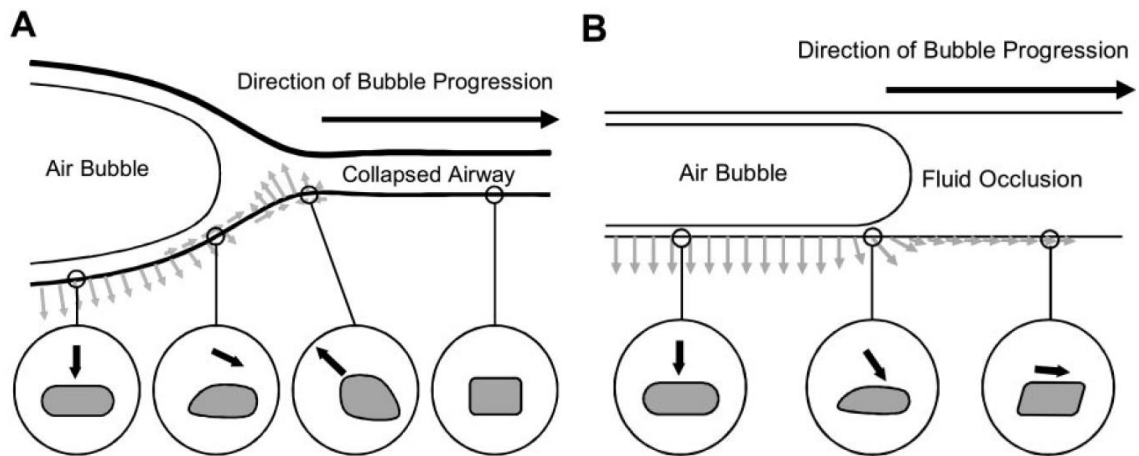


Figure 2.7: Hypothetical stresses on epithelial cells during airway reopening in A) a collapsed compliant airway and B) a fluid-occluded rigid channel. For the collapsed compliant airway, cells far downstream of the bubble experience nominal stress. As the bubble approaches the cell is pulled toward the bubble, and as the bubble passes the cell is pushed away from the bubble. After the bubble has passed, the cell experiences an outward normal stress. For the fluid-occluded rigid channel, cells far downstream experience a forward tangential stress. As the bubble approaches the cell is pushed forward, and once the bubble passes the cell experiences an outward normal stress (Bilek *et al.*, 2003).

by mechanotransduction, leading to the activation of cell-signaling pathways that initiate and propagate a systemic inflammatory response (Slutsky and Tremblay, 1998).

Therefore mechanical stresses associated with airway reopening can have profound effects on epithelium, warranting further investigation.

During airway reopening, the Law of Laplace ($\Delta P = 2\gamma/R$, where ΔP is the pressure drop, γ is surface tension, and R is the radius of curvature) governs the yield pressure drop across the interface that initiates the progression of the bubble due to surface tension. For compliant airways, the yield pressure was previously thought to be equal to twice the surface tension divided by the open airway radius ($2\gamma/R$) as described by the Law of Laplace. However, Gaver *et al.* demonstrated that due to the complexity of the radius of curvature, the opening pressures of airways with low capillary number are mostly determined by surface tension and follow $P_{cap} \approx 8\gamma/R$ (1990). Notice that the pressure drop can become very large as the radius of the spherical interface becomes small, and that flexibility can reduce the radius of curvature (**Figure 2.7**). This indicates that small peripheral airways are more susceptible to large pressure gradients during the recruitment and derecruitment of occluded airways.

Surface tension and viscosity of the airway lining fluid also play an important role in determining the pressure required to open a collapsed compliant airway, and the relative importance of viscous and surface tension forces is represented by the capillary number ($Ca = \mu U/\gamma$, where μ is the viscosity, U is the reopening velocity, and γ is the surface tension). At small capillary numbers, the surface tension dominates and the pressure required to propagate the meniscus at a velocity U is determined by the pressure drop across the interface. As the capillary number increases, the viscosity of the lining

fluid begins to retard the motion of the meniscus, and greater opening pressures are required (Gaver *et al.*, 1990). This is important when considering the recruitment and derecruitment of collapsed compliant tubes.

2.7 Evidence for Epithelial Cell Damage

It is difficult to determine the mechanism of damage during airway reopening in whole lung models due to the complex spatial and temporal environment. For this reason, *in vitro* models have been employed to analyze the effect of mechanical stresses during airway reopening on the pulmonary epithelium. Because the mechanical environment is associated with a two-phase (air-liquid) interfacial flow, the mechanics governing a single-phase steady flow (such as in vascular studies) do not provide a suitable description. The progressing air-liquid interface that reopens an occluded airway creates significant spatial and temporal gradients in shear and normal stress that may contribute to VILI. It has been repeatedly demonstrated that these forces are sufficient to induce pulmonary epithelial membrane rupture (Bilek *et al.*, 2003; Kay *et al.*, 2004; Yalcin *et al.*, 2007; Huh *et al.*, 2007; Yalcin *et al.*, 2009; Oeckler *et al.*, 2010; Douville *et al.*, 2011; Glindmeyer *et al.*, 2012; Jacob and Gaver, 2012; Higuera-Castro *et al.*, 2014). The methods and conclusions of the most relevant studies are summarized in **Table 2.1**.

Bilek *et al.* observed that cells exposed to small Ca interfacial flows experience higher levels of cellular injury and that the addition of pulmonary surfactant reduces this injury to similar levels as controls (2003). They found that the increase in epithelial damage with low Ca corresponds to an increased pressure gradient. Kay *et al.* built on this analysis by modifying the viscosity of the occlusion fluid without changing velocity to demonstrate that the pressure gradient and not the exposure duration, determines the

Author	Cell Host / Type	Apparatus	Full Channel Height (mm)	Velocity (mm/s)	Variables
Bilek et al., 2003	Rat / CCL-149	Parallel-plate	1.7	≈ 3 ≈ 30	<ul style="list-style-type: none"> • PBS solution • Pulmonary surfactant solution
Conclusions: <ul style="list-style-type: none"> • Decreasing the capillary number increases cellular injury • Pulmonary surfactant reduces cellular injury to similar levels as control • Cellular injury is associated with the pressure gradient during the "stress cycle" 					
Kay et al., 2004	Human / A549	Parallel-plate	1.7	≈ 3.4	<ul style="list-style-type: none"> • PBS (low viscosity) • PBS + Dextran (high viscosity)
Conclusions: <ul style="list-style-type: none"> • Pressure gradient, not exposure duration, determines mechanical damage • Cyclic recruitment and derecruitment (1, 5, 20 cycles) results in substrate denudation 					
Yalcin et al., 2007	Rat / CCL-149	Parallel-Plate	0.5 0.8 1.7	0.3 3 30	<ul style="list-style-type: none"> • Low confluence • High confluence • 1, 3, or 5 bubble passes
Conclusions: <ul style="list-style-type: none"> • Decreasing channel height and decreasing reopening velocity increases cellular injury • Low-confluence monolayers experience increased cellular injury • After a critical number of bubble passes, the bubble does not induce additional cellular injury 					
Yalcin et al., 2009	Human / A549	Parallel-plate	0.5	3	<ul style="list-style-type: none"> • Jasplakinolide (stabilize actin) • Latrunculin A (depolymerize actin) • 23°C or 37°C
Conclusions: <ul style="list-style-type: none"> • Decreasing cell elastic modulus due to actin depolymerization reduces cellular injury • Actin depolymerization resulted in improved cell adhesion but weaker focal adhesions • Experiments at 37°C exhibit significantly reduced cellular injury 					
Oeckler et al., 2010	Human / A549	Microfluidic Chamber		2	<ul style="list-style-type: none"> • hypotonic (250 mOsm) HMEM • isotonic (290 mOsm) HMEM • hypertonic (340 mOsm) HMEM
Conclusions: <ul style="list-style-type: none"> • Hypertonic solution reduced cellular injury and hypotonic solution increased cellular injury 					
Glindmeyer et al., 2012	Human / H441	Silicone Tube	1.6	Reverse Flow Reopening Waveform	<ul style="list-style-type: none"> • Surfactant free • 0.1 mg/mL surfactant • 1.0 mg/mL surfactant • 1.0 mg/mL surfactant + 5.0 mg/mL albumin
Conclusions: <ul style="list-style-type: none"> • Flow reversal with surfactant reduced cellular injury compared to surfactant free • Cell protection may persist beyond flow reversal, suggesting downstream enriched surfactant transport 					
Jacob and Gaver, 2012	Human / H441	Parallel-plate	1.7	2.7 27	<ul style="list-style-type: none"> • Ouabain (paracellular permeability) • Ethidium Homodimer-1 (plasma membrane permeability)
Conclusions: <ul style="list-style-type: none"> • Decreasing the velocity of reopening significantly augments pulmonary epithelial barrier dysfunction • The apical pressure gradient transmits through the cell to induce large basolateral tangential gradients 					
Higueta-Castro et al., 2014	Human / A549 Human / HSAEpC	Parallel-plate	0.5	0.3	<ul style="list-style-type: none"> • 3.4-kPa elastic modulus substrate • 10.6-kPa elastic modulus substrate • 68.6-kPa elastic modulus substrate
Conclusions: <ul style="list-style-type: none"> • Increases in substrate stiffness resulted in increased cellular necrosis and decreased cell detachment 					

Table 2.1: A brief summary of methods and conclusions from relevant *in vitro* experiments on airway reopening.

amount of epithelial damage (2004). These two studies concluded that pressure gradient is the primary stimulus responsible for inducing cellular injury during airway reopening.

After concluding the damaging mechanism is pressure gradient, studies began to focus on methods of protecting epithelium from cellular injury. Yalcin *et al.*

demonstrated that a high-confluence monolayer experiences significantly lower cellular injury compared to a low-confluence monolayer (2007). In a later study, Yalcin *et al.*

demonstrated that decreasing the cell's elastic modulus by depolymerizing actin reduces the epithelial damage (2009). In addition, they explored the effects of temperature on

cellular injury from interfacial flows and concluded that experiments at 37°C exhibit significantly lower injury than at 23°C. Oeckler *et al.* found that tonicity of occlusion

fluid is another factor that can affect cellular injury (2010). In this study, hypertonic occlusion fluid reduced cellular injury while hypotonic fluid increased cellular injury

compared to an isotonic control. Glindmeyer *et al.* investigated the effects of flow reversal, and they found that cell protection persists beyond retrograde motion,

suggesting downstream enriched surfactant transport (2012). Jacob *et al.* analyzed

paracellular permeability, finding that decreasing the velocity of reopening augments epithelial barrier dysfunction (2012). Through computational modeling they also

determined that the pressure gradient imposed on the apical membrane of the cell transmits through the cell to induce a large tangential gradient on the basolateral

membrane. Finally Higuera-Castro *et al.* explored the effect of compliant substrates on epithelial damage and found that increasing substrate stiffness results in increased

cellular necrosis and decreased cell detachment (2014). While these *in vitro* experiments only approximate the true physiology of airway recruitment and derecruitment, they

contribute valuable insight that can inform clinical practice for treating patients with collapsed and occluded airways.

The vast majority of *in vitro* models have focused on epithelial cell damage resulting from a single airway reopening event. Although patients are cyclically ventilated for many breaths, previous studies have demonstrated minimal evidence for trends in epithelial damage with increasing number of airway recruitment and derecruitment cycles. In 2004, Kay *et al.* qualitatively showed that cyclic recruitment and derecruitment for 1, 5, and 20 cycles leads to significant cellular detachment and denudation of the substrate. Yalcin *et al.* quantitatively investigated the cellular injury associated with 1, 3, and 5 recruitment-derecruitment cycles, and they concluded that between 3 and 5 bubble passes there is a critical number of passes where the interfacial flow does not induce additional cellular injury. This suggests that cellular injury has asymptotic behavior with an increasing number of recruitment-derecruitment cycles, providing the motivation for the current study. The current study explores the trends of cellular injury and detachment associated with 1, 5, 10, 15, and 20 cycles of airway recruitment and derecruitment.

2.8 Project Rationale

The overall goal of this research is quantify the magnitude of cellular injury and detachment associated with interfacial stresses that arise from cyclic progression and retraction of an air-liquid interface through an *in vitro* airway occlusion model. To accomplish this goal, we developed a longitudinal study to investigate the behavior of specific cell populations within models of pulmonary airways after an increasing number

of sequential recruitment-derecruitment events, and we have completed the following specific aims:

2.8.1. Specific Aim 1: Establish a rigid in vitro model of cyclic recruitment and derecruitment using human lung epithelial cells.

We develop a pulmonary airway model with cylindrical geometry using rigid glass tubing and culture a confluent monolayer of human lung epithelial cells within the tube to investigate the biological impact of airway reopening. The biological relevance of the model is validated by passing a single semi-infinite bubble of air through the occluded airway at pre-determined velocities and comparing the results to prior models of airway recruitment.

2.8.2. Specific Aim 2: Quantify the cellular injury associated with an increasing number of recruitment and derecruitment cycles.

We use our airway model from specific aim 1 to investigate the biological effects associated with multiple cycles of recruitment and derecruitment, as opposed to a single airway reopening event. Cellular membrane permeability serves as a metric of epithelial damage due to mechanical stresses, consistent with previous studies (**Table 2.1**).

Pulmonary surfactant is incorporated into the model to mimic more physiologically relevant conditions.

2.8.3. Specific Aim 3: Track the cellular injury and detachment longitudinally with progressing number of airway recruitment and derecruitment cycles.

We implement a novel technique of tracking the same experimental tube longitudinally with progressing number of recruitment and derecruitment cycles to accurately assess the magnitude of cellular detachment. This assessment informs us

whether quantifying cellular injury of attached cells alone is a biased estimator of the system's biological response. We compare our findings to the qualitative results of Kay *et al.* (2004) and the quantitative results of Yalcin *et al.* (2009).

3. MATERIALS AND METHODS

3.1 Introduction

Pulmonary airway reopening by mechanical ventilation results in ventilator-induced lung injury (VILI), which can damage the epithelium of airways with a progressing air-liquid interface. Previous studies have demonstrated that interfacial flows produce significant mechanical stresses capable of rupturing cell membranes and detaching cells from their substrate (**Table 2.1**). Most airway reopening experiments have been conducted in parallel plate chambers, but Glindmeyer *et al.* developed an *in vitro* model using silicone tubing that more closely mimics the three-dimensional cylindrical geometry of a terminal bronchiole (2012). The goal of the current study is to expand on this cylindrical rigid model and investigate the biological effects of cyclic recruitment and derecruitment with multiple bubble passes.

To begin, we developed a method of seeding human NCI-H441 lung epithelial cells (ATCC, Manassas, VA) in glass tubes with a physiologically-relevant diameter. We designed an acrylic syringe holder to mount air-filled syringes to a linear motor capable of producing oscillatory motion. Pulmonary surfactant was introduced into the model to lower surface tension and to more accurately represent the *in vivo* environment. To analyze the number of seeded cells, detached cells, and dead cell, fluorescent dyes were added to the occlusion fluid of experimental tubes and imaged using an inverted epifluorescence microscope. To characterize the total number of cells present in the glass tube prior to airway reopening, flow cytometry data was collected for both forward

scatter and side scatter. This section details the materials and methods required for the development of our cyclic recruitment and derecruitment model.

3.2 Materials

3.2.1 Fibronectin

Human plasma fibronectin (Gibco, Grand Island, NY) is a primary cell adhesion molecule and exhibits structural and adhesive properties in cell-associated fibrillar matrices. Fibronectin is commonly used to coat tissue culture dishes, aiding in cell adhesion. Because the glass tubes used in this study were untreated when purchased, fibronectin treatment was necessary to promote cell adhesion to the glass. Glass tubes were coated with a solution of 150 μ g/mL fibronectin (see **section 3.3.2** on tube pre-treatment), matching the study conducted by Glindmeyer *et al.* (2012).

3.2.2 Infasurf

Infasurf (ONY Inc, Amherst, NY) is a naturally-derived pulmonary surfactant from calf lungs (calfactant) which includes phospholipids, neutral lipids, and hydrophobic surfactant-associated proteins B and C (SP-B and SP-C). It rapidly adsorbs into the surface of the air-liquid interface and modifies alveolar surface tension, similar to natural lung surfactant. Infasurf is an off-white suspension of calfactant in 0.9% aqueous sodium chloride solution with a pH range of 5.0 – 6.2. Each bottle of Infasurf contains 6mL of solution with a 35mg/mL total phospholipid concentration; however, the standard model of interfacial behavior in our laboratory has previously used a 1mg/mL concentration of phospholipid Infasurf. Infasurf was obtained by a generous donation from ONY Inc, and each bottle was stored in a -20°C freezer until ready for use. Once thawed, each bottle of Infasurf was stored in a refrigerator for up to 4 weeks.

3.2.3. Hoechst Stain

Hoechst 33342 is a fluorescent molecular probe that emits blue fluorescence when bound to nucleic acids. This probe is cell-permeant, so it is used in this study to stain the DNA in the nucleus of all cells. Images are taken of Hoechst-stained cells using fluorescence microscopy and merged with images of the same cells stained with other molecular probes to distinguish between cell populations. The excitation and emission maxima are 350nm and 461nm respectively, and the full fluorescence spectrum is shown in part A of **Figure 3.1**. A Nikon UV-2A ultraviolet excitation filter (Melville, NY) with 330-380nm bandpass excitation and 420nm cut-on longpass emission (barrier) filter was used to collect the fluorescence from ultraviolet excitation of Hoechst 33342.

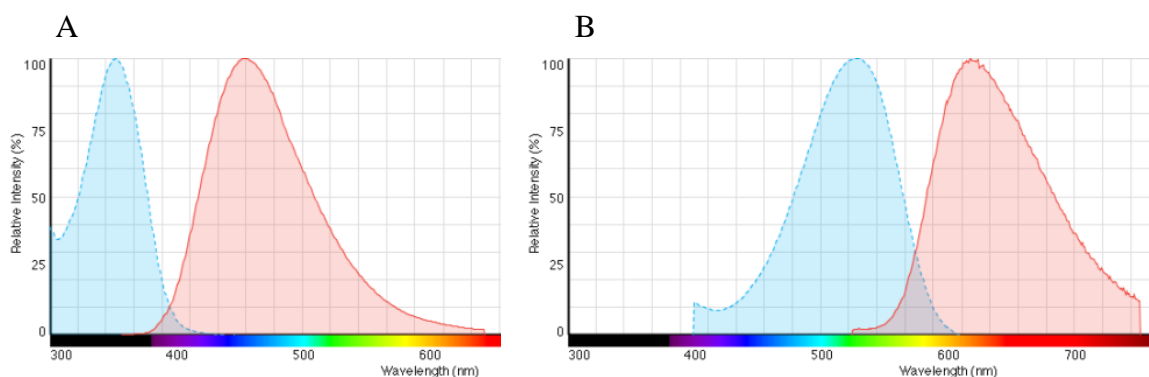


Figure 3.1: Fluorescence spectra of A) Hoechst 33342 and B) Ethidium Homodimer-1 according to the manufacturer, ThermoFisher Scientific.

3.2.4. Ethidium Homodimer-1 Stain

Ethidium Homodimer-1 is a fluorescent molecular probe that weakly emits red fluorescence until bound to nucleic acids. When Ethidium Homodimer-1 binds to DNA it strongly emits red fluorescence. The excitation and emission maxima are 528nm and

617nm respectively, and the full fluorescence spectrum is shown in part B of **Figure 3.1**.

A Nikon G-2A green excitation filter (Melville, NY) with 510-560nm bandpass excitation and 590nm cut-on longpass emission (barrier) filter was used to collect the fluorescence from green excitation of Ethidium Homodimer-1. In contrast to the Hoechst stain, Ethidium Homodimer-1 is cell-impermeant, meaning that the molecule cannot cross a cell's plasma membrane unless the plasma membrane is ruptured. For this reason the Ethidium Homodimer-1 stain is used in this study to stain the DNA in the nucleus of dead cells and cells with ruptured plasma membranes. Images are taken of Ethidium-stained cells using fluorescence microscopy and merged with images of the same cells stained with other molecular probes to distinguish between cell populations.

3.2.5. Acrylic Syringe Holder

A syringe holder was designed to secure the barrel of the syringe to a fixed rail while securing the plunger of the syringe to the shaft of a linear motor (PS01-23x80, LinMot, Elkhorn, WI) as shown in **Figure 3.2**. This allows the programmable motion of the linear motor to be directly translated to the plunger of the syringe. By altering the waveforms that drive the motion of the linear motor, the flow rate of the fluid leaving syringe can be precisely controlled. The syringe holder was manufactured from a 1/4" thick piece of flat poly(methyl methacrylate), also known as PMMA or acrylic. The design was cut using an Epilog laser cutter (Golden, CO) and assembled using acrylic solvent cement (SCIGRIP, Durham, NC).

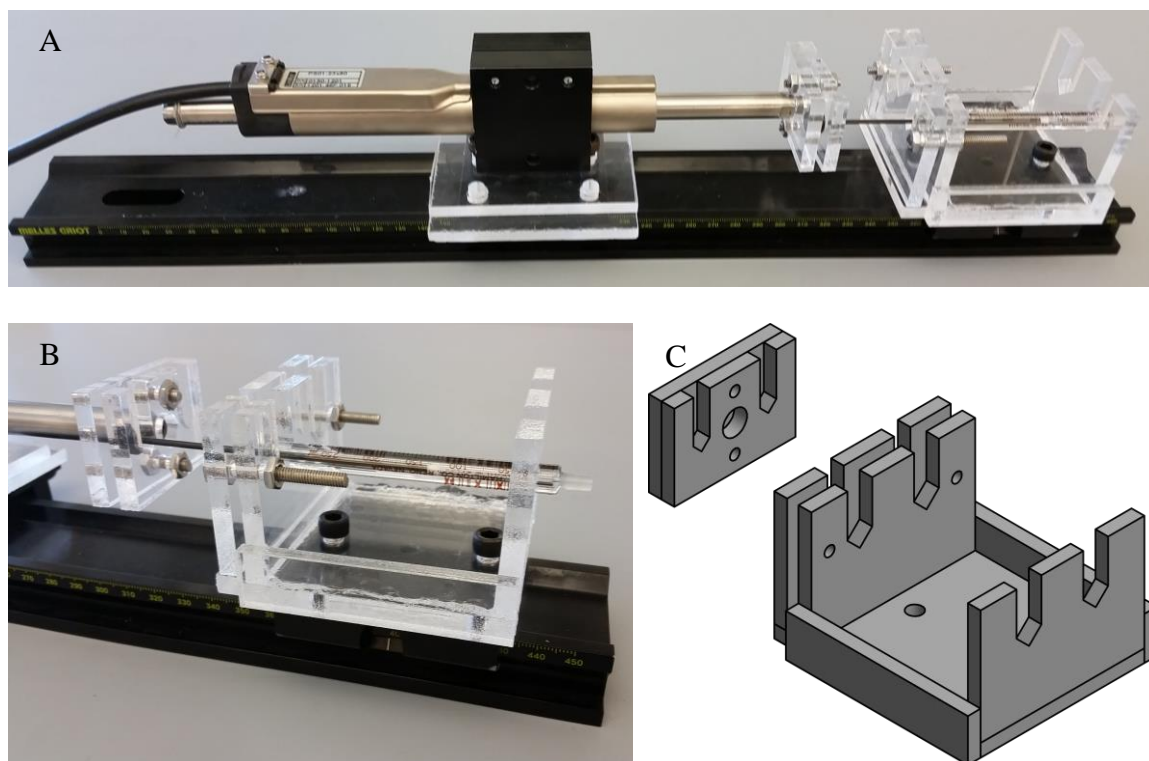


Figure 3.2: Acrylic syringe holder to translate the motion of the linear motor to the plunger of the gas-tight syringe. A) The syringe holder attached to the linear motor. B) A view of the holder with a syringe in place. C) The computer-aided drawing of the syringe holder used for laser cutting.

3.2.6. Glycerol

Glycerol, also known as glycerine, is a non-toxic alcohol compound with three hydroxyl groups. It has a relatively high viscosity and is readily soluble in water. The most important properties of glycerol for this application are that it is optically clear and its refractive index is approximately 1.475, which more closely matches the refractive index of borosilicate glass when compared to water or air (**Table 3.1**). For this reason, 99.5% purified glycerol was used as a refractive index matching liquid to create optical coupling between the microscope slide and glass tube during fluorescence microscopy (**Figure 3.3**). The glass tube was submerged in 99.5% glycerol using the experimental tube holder during to image acquisition to reduce distortion.

Material	Approximate Refractive Index
Air	1.000
Water	1.333
Glycerol	1.475
Borosilicate Glass	1.517

Table 3.1: Approximate refractive indices for materials used in experimental setup during fluorescence microscopy.

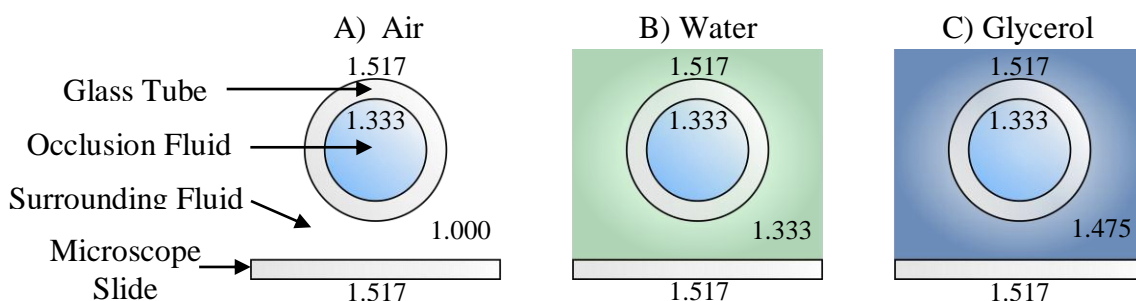


Figure 3.3: The use of glycerol for optical coupling is better than either air or water. A) Experimental tube with no coupling fluid. B) Experimental tube submerged in water for optical coupling. C) Experimental tube submerged in glycerol for optical coupling.

3.2.7. Experimental Tube Holder

The experimental tube holder (**Figure 3.4**) was designed to hold the cell-seeded experimental tube in a fixed position on the microscope stage and allow it to be submerged in glycerol without harming the microscope. The experimental tube holder consists of a standard 2" x 3" microscope slide (Fisher Scientific, Houston, TX), replaceable cord weatherstrip (M-D Building Products, Oklahoma City, OK), the experimental tube, and 99.5% glycerol. To assemble the tube holder, a 10inch long piece of cord weatherstrip was cut off of the roll, and folded in half so that four cords were visible along the height of the weatherstrip. The folded weatherstrip was then bent to match the outline of the microscope slide and pressed firmly to adhere it to the slide. Scissors were used to cut a rectangular section through 3 out of the 4 cords on both of the 2" sides, as shown in part A of **Figure 3.4**. The experimental tube was then placed in the

rectangular openings, and the rectangular plugs from the cuts were used to fill the gap (part B of **Figure 3.4**). The pair of scissors were then used to smooth the inside surface of the weatherstrip around the glass tube, closing any small holes or cracks. Finally, the holder was filled with glycerol and placed on the microscope stage for image acquisition.

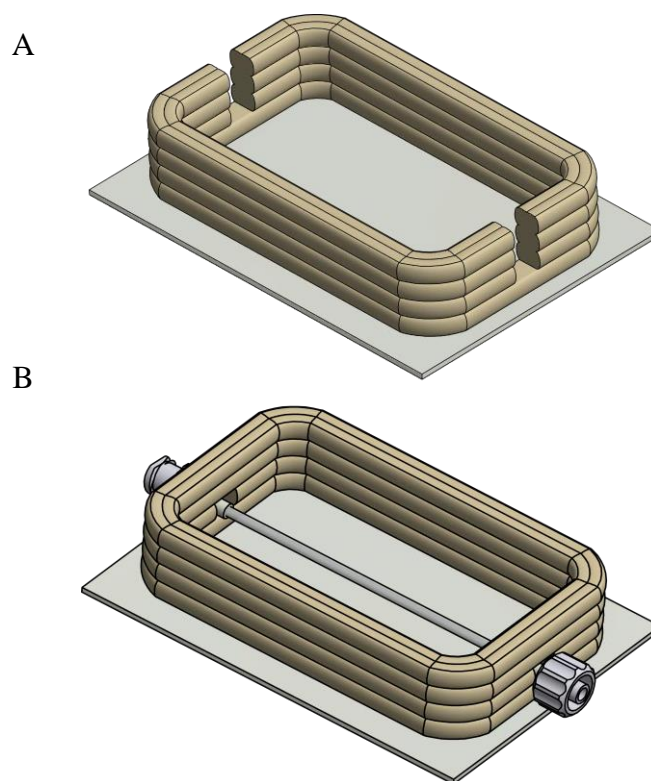


Figure 3.4: The experimental tube holder designed to secure the experimental tube while submerging it in glycerol for optical coupling. A) A rectangular cut in the cord weatherstrip is made to slide the experimental tube into the holder. B) Once the experimental tube is in place, the plugs of cut weatherstrip are replaced and smoothed over with scissors to remove any gaps in the weatherstrip seal against the tube.

3.3 Methods

3.3.1. Epithelial Cell Subculture

Human NCI-H441 pulmonary epithelial cells were purchased from ATCC (Manassas, VA) and cryopreserved in liquid nitrogen. This cell line was chosen because it has been shown to be suitable for in vitro models of distal lung epithelium (Salomon *et al.*, 2014). It has also been used previously in this laboratory by Jacob *et al.* (2012),

Glindmeyer *et al.* (2012), and Harrison (2015), allowing for comparison of results.

Epithelial cells were thawed and routinely cultured in 175 cm² growth area tissue culture flasks (Corning, Tewksbury, MA). The flasks were stored in a humidified incubator at 37°C with 5% carbon dioxide and replaced on a weekly basis. Growth media was exchanged daily and consisted of RPMI-1640 medium (ATCC, Manassas, VA) supplemented with 10% fetal bovine serum (ATCC, Manassas, VA), and 2% Antibiotic-Antimycotic (Gibco, Grand Island, NY). When the NCI-H441 cells reached approximately 80% confluence, they were passaged using Trypsin-0.25% EDTA (ThermoFisher Scientific, Grand Island, NY) to avoid overcrowding.

3.3.2. Tube Pre-treatment

Borosilicate glass tubes with an inner diameter of 1.56mm and an outer diameter of 2.00mm were purchased from Sutter Instrument Co. (Novato, CA). The glass tubes with an original length of 15cm were cut in half using a handheld diamond glass cutter to create tube lengths of approximately 7.5cm. To attach 1/16" nylon female and male barbed luers to the glass tube, small segments of 1/16" inner diameter and 1/8" outer diameter silicone tubing (Cole-Parmer, Vernon Hills, IL) were placed over each end of the glass tube to produce the experimental tube shown in **Figure 3.5**.

Once the experimental tubes were assembled, they were sterilized in an acid solution of H₂O/H₂O₂/HCl in a volume ratio of 5:1:1 proposed by Sui *et al.*, (2006). The acid solution was injected into each tube using a 10mL disposable syringe (BD, Franklin Lakes, NJ) and allowed to rest for 15 minutes under a chemical fume hood. The acid solution was subsequently ejected and flushed 3 times with deionized water to neutralize residual acid.

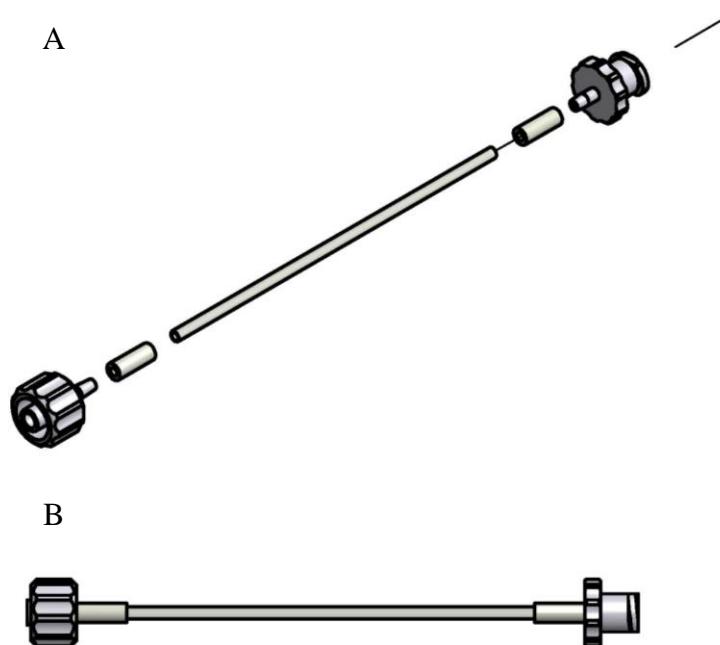


Figure 3.5: Experimental tube for cell seeding. A) Exploded view of all components. Listed from left to right the components are: female barbed luer, silicone tubing, borosilicate glass tube, silicone tube, and male barbed luer. B) Assembled tube.

The experimental tubes were then placed under a laminar flow hood and a solution of 150 μ g/mL of human plasma fibronectin (Gibco, Grand Island, NY) in Dulbecco's Phosphate Buffered Saline + Calcium Chloride + Magnesium Chloride (Gibco, Grand Island, NY) was pipetted into the experimental tubes. The tubes were then placed in a humidified incubator at 37°C with 5% carbon dioxide for 1 hour, rotated 180 degrees, and placed back in the humidified incubator for another hour.

3.3.3. Seeding Glass Tubes with Epithelial Cells

After 2 hours of human plasma fibronectin treatment, the experimental tubes were ready to be seeded with cells according to the following protocol:

- 1) The growth media from the 175 cm² growth area tissue culture flask of NCI-H441 cells was removed and 5mL of Trypsin-0.25% EDTA (ThermoFisher

Scientific, Grand Island, NY) was pipetted into the flask. The flask was placed in a humidified incubator at 37°C with 5% carbon dioxide for 10 minutes.

- 2) After cell detachment was confirmed under a microscope, the Trypsin-cell suspension was transferred to a 15mL centrifuge tube (Nunc, Rochester, NY) and 5 mL of growth media was added to the suspension, creating a 1:1 ratio. The addition of growth media is important to deactivate the enzymatic activity of the Trypsin.
- 3) A 10µL sample of the Trypsin-cell-growth media suspension was removed for cell counting using a standard hemocytometer. The remainder of the suspension in the 15mL centrifuge tube was capped and placed in a Heraeus Multifuge X3R centrifuge (ThermoFisher, Am Kalkberg, Germany) with the following settings: acceleration = 9, deceleration = 9, speed = 130g, time = 5mins, temperature = 20°C.
- 4) While centrifuging, the 10µL suspension sample was combined with 10µL of Trypan Blue (Gibco, Grand Island, NY) and pipetted into a hemocytometer slide. The cell concentration was calculated according to the equation:

$$\text{Cell Concentration} \left(\frac{\text{cells}}{\text{ml}} \right) = \left(\frac{\text{Average \# of cells}}{100 \text{ nl quadrant}} \right) \left(\frac{1 \times 10^6 \text{ nl}}{\text{ml}} \right) (\text{Dilution}).$$
This concentration was used to calculate the volume of growth media required to achieve a cell concentration of 2.5×10^6 cells/mL in the final suspension.
- 5) After centrifuging, the supernatant was removed from the 15mL centrifuge tube, the calculated volume of growth media was added to the tube, and the cells were re-suspended by hand pipetting to a final concentration of 2.5×10^6 cells/mL.

- 6) Using a 1000 μ L micropipetter, the cell suspension was pipetted into the fibronectin-treated experimental tubes, ejecting the remaining excess of fibronectin solution. These cell-seeded tubes were then placed in a humidified incubator at 37°C with 5% carbon dioxide for 2 hours.

3.3.4. Media Perfusion

After 2 hours of allowing the cells to settle and adhere to the bottom of the experimental tube, the tubes were ready to be perfused with media for 22 hours.

- 1) Using a 1000 μ L micropipetter, new growth media was pipetted into the cell-seeded experimental tubes, ejecting the remaining excess of cell suspension. This liquid transfer was pipetted carefully to avoid introducing air bubbles.
- 2) The perfusion apparatus in **Figure 3.6** was assembled, starting with the perfusion tube. For each experimental tube, a perfusion tube was created by attaching one 1/16" nylon female or male luer to each end of a 1/16" inner diameter and 1/8" outer diameter silicone tube (Cole-Parmer, Vernon Hills, IL) with a length of approximately 1 meter.
- 3) A serological pipette was used to completely fill the perfusion tube with new growth media.

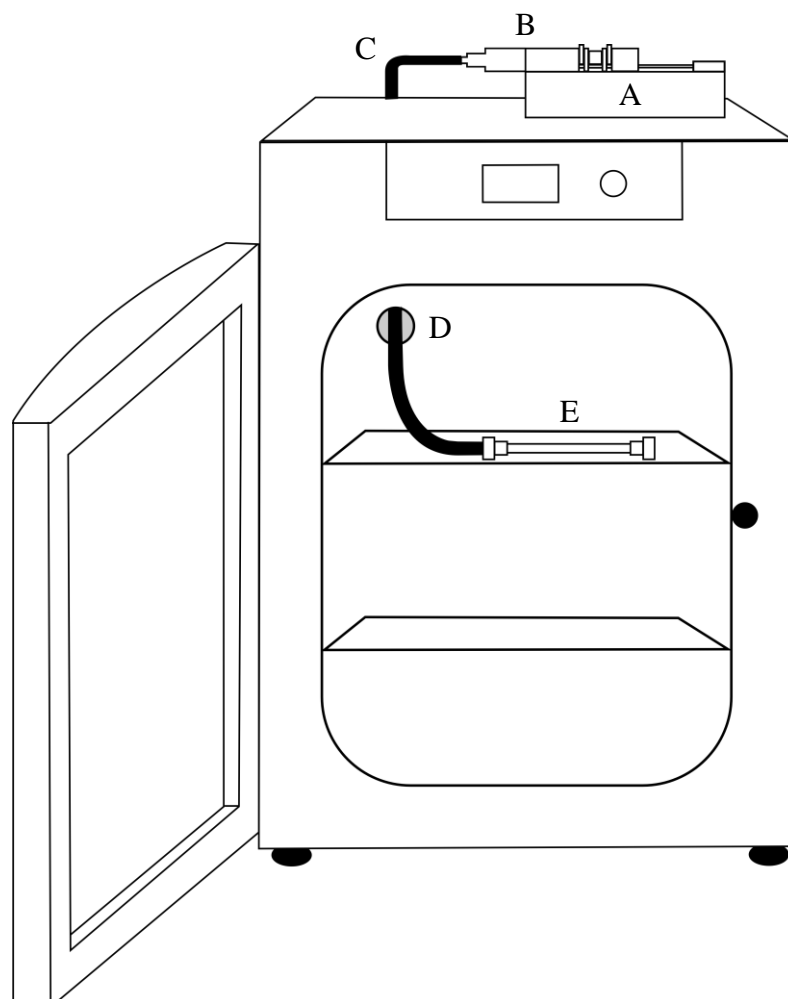


Figure 3.6: Perfusion apparatus for perfusing new media into cell-seeded experimental tubes. A) Syringe pump. B) 5mL disposable syringe. C) Perfusion tube consisting of approximately 1 meter of Silicone tubing with a male or female luer on each end. D) Rear access port to the incubator. E) Experimental tube.

- 4) The media-filled perfusion tube was attached directly to the experimental tube by locking the male and female luers together. To avoid bubbles, both luers were flooded with growth media and gently locked together as shown in **Figure 3.7**.
- 5) A two-way stopcock was attached to the opposite end of experimental tube to allow closure of the system during transport.

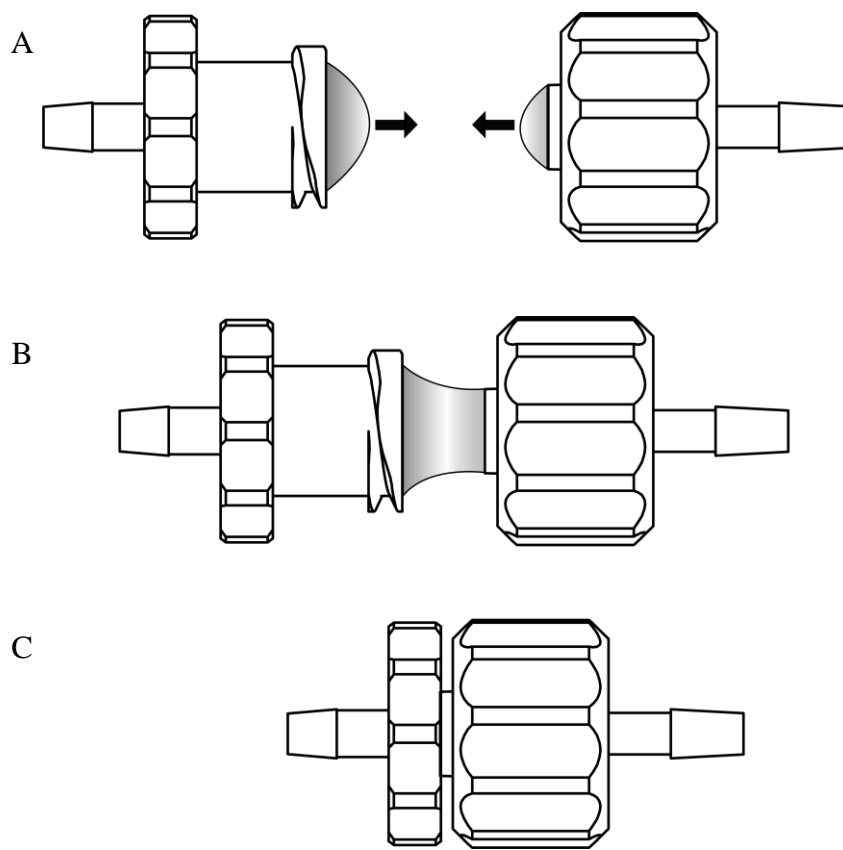


Figure 3.7: How to assemble male and female luers without introducing air bubbles into the system. A) Both the male and female luers are completely filled with liquid so that a meniscus extends past the luer opening. B) The luers are slowly moved toward each other so that the two menisci join together. C) The luers are locked tightly together to complete the assembly.

- 6) For each experimental tube, a 5 mL disposable syringe was filled with deionized water and connected to the 74900 series ten-syringe infusion pump (Cole-Parmer, Vernon Hills, IL). The syringe pump was programmed for the corresponding diameter of the 5mL disposable syringe and set to a flow rate of $Q = 50\mu\text{L}/\text{hour}$, suggested by Huh *et al.* (2012). The syringe pump and syringe were placed on top of the incubator.
- 7) The two-way stopcock on the end of the experimental tube was closed, and

the perfusion and experimental tubes were placed inside the incubator.

- 8) The perfusion tube was pulled through the rear access port on the incubator, shown in **Figure 3.6**, and attached to the syringe and syringe pump on top of the incubator.
- 9) Once the perfusion apparatus was complete, the syringe pump was started.

Growth media was allowed to flow for 22 hours before experimentation.

3.3.5. Single Recruitment Experimental Protocol

After 22 hours of media perfusion (24 hours post-seeding with cells), the experimental tubes were removed from the perfusion apparatus. The single recruitment experiment was conducted according to the following protocol.

- 1) Using a 1000 μ L micropipetter, Dulbecco's Phosphate Buffered Saline + Calcium Chloride + Magnesium Chloride (DPBS++) (Gibco, Grand Island, NY) was pipetted into the experimental tube, ejecting the growth media from perfusion. The DPBS++ serves as the occlusion fluid for the airway model, and the liquid transfer was pipetted carefully to avoid introducing air bubbles.
- 2) A staining solution of 5 μ M Hoechst (Life Technologies, Grand Island, NY) and 5 μ M Ethidium Homodimer-1 (Life Technologies, Grand Island, NY) in DPBS++ was prepared for staining all cells and cells with compromised plasma membranes, respectively. Infasurf pulmonary surfactant (ONY Inc, Amherst, NY) was added to the staining solution at a concentration of 1mg/mL to minimize cellular damage during the mandatory staining solution derecruitment.

- 3) The DPBS++ occluded experimental tube was removed from the laminar flow hood and transported to the workbench, where it was connected to the air-filled upstream tube and air-filled downstream tube using 1/16" nylon luers (Cole-Parmer, Vernon Hills, IL) and the technique shown in **Figure 3.7**. Both the upstream and downstream tubes were 1/16" inner diameter and 1/8" outer diameter silicone tubing (Cole-Parmer, Vernon Hills, IL) with an approximate length of 12 inches.
- 4) The air-filled upstream tube was attached to a model 1001 1mL gas-tight syringe (Hamilton Company, Reno, NV), which was placed in a 74900 series ten-syringe infusion pump (Cole-Parmer, Vernon Hills, IL). The syringe pump was programmed for the corresponding diameter of the 1mL gas-tight syringe and set to a flow rate of either $Q = 3.016\text{mL/min}$ or $Q = 0.302\text{mL/min}$, depending on the experimental group. The result was an experimental setup identical to part A of **Figure 3.8**.
- 5) The syringe pump was turned on, displacing the occlusion fluid in the experimental tube with a semi-infinite bubble of air from the upstream tube. This resulted in a recruitment event for the in-vitro airway model. The syringe pump was turned off once all of the occlusion fluid was displaced forward into the downstream tube (part B of **Figure 3.8**).
- 6) The upstream tube was then disassembled and replaced with a new upstream tube. Staining solution was carefully pipetted into the new upstream tube and the tube was reassembled using the technique shown in **Figure 3.7** (resulting in part C of **Figure 3.8**). Replacing the upstream tube was necessary to ensure

that no pulmonary surfactant remained in the liquid lining of tube, potentially affecting subsequent experimental trials. For this reason, one upstream tube was dedicated to air and another to solutions containing surfactant.

- 7) The syringe pump was turned on with a fast flow rate of $Q = 3.016\text{mL/min}$ to displace the staining solution forward, resulting in a mandatory derecruitment event as shown in part D of **Figure 3.8**. Once the staining solution completely filled the experimental tube, the syringe pump was turned off. A fast flow rate was always used to introduce the stain-surfactant solution, because Glindmeyer *et al.* (2012) demonstrated that higher recruitment velocities resulted in lower cellular damage in a rigid tube model.

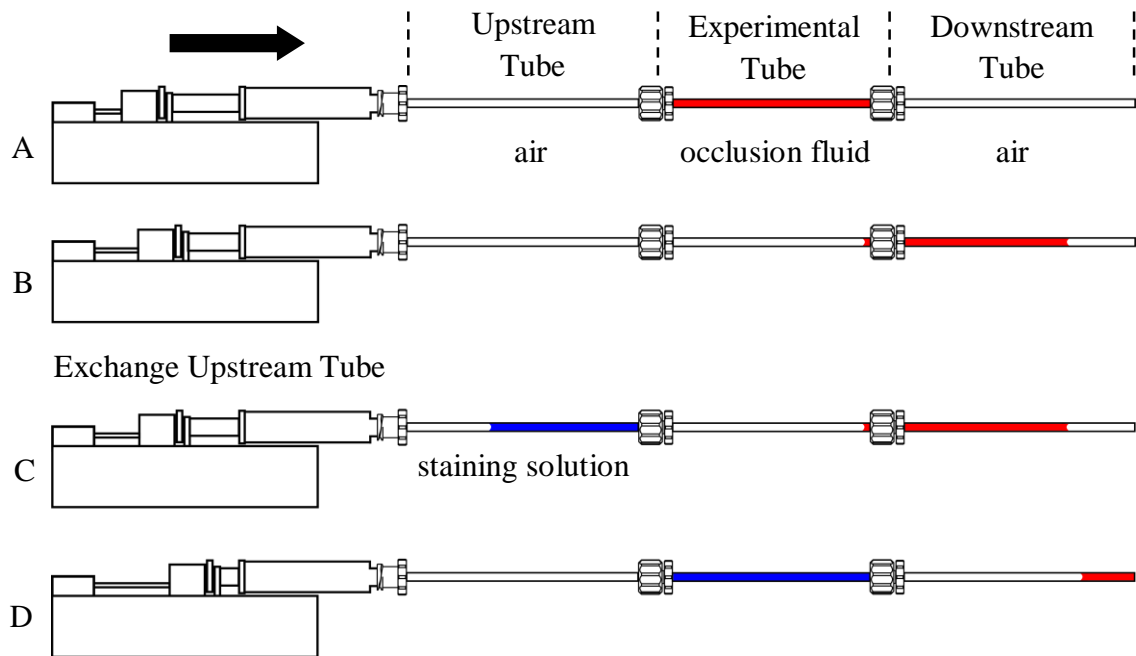


Figure 3.8: Movement of fluids at different time points during the single recruitment experiment. A) The occlusion fluid fills the experimental tube seeded with cells. B) Air from the upstream tube is displaced forward by the syringe pump, creating a recruitment event. C) The upstream tube is exchanged for tube filled with staining solution. D) The staining solution from the upstream tube is displaced forward by the syringe pump, creating a derecruitment event. The staining solution contains pulmonary surfactant to reduce the cellular damage associated with this mandatory derecruitment.

- 8) Once the experimental tube was filled with staining solution, the experimental tube was disassembled from experimental apparatus and placed in a humidified incubator for 15 mins at 37°C with 5% carbon dioxide.
- 9) The experimental tube was then removed from the incubator for imaging.

3.3.6. Cyclic Recruitment-Derecruitment Experimental Protocol

After 22 hours of media perfusion (24 hours post-seeding with cells), the experimental tubes were removed from the perfusion apparatus. The cyclic recruitment / derecruitment experiment was conducted according to the following protocol.

- 1) A staining solution of 5µM Hoechst (Life Technologies, Grand Island, NY) and 5µM Ethidium Homodimer-1 (Life Technologies, Grand Island, NY) in DPBS++ was prepared for staining all cells and cells with compromised plasma membranes, respectively. Infasurf pulmonary surfactant (ONY Inc, Amherst, NY) was added to the staining solution at a concentration of 1mg/mL to minimize cellular damage during the mandatory staining solution derecruitment.
- 2) Using a 1000µL micropipetter, the staining solution was pipetted into the experimental tube, ejecting the growth media remaining from perfusion with care to avoid introducing air bubbles. The staining solution serves as the occlusion fluid for the airway model.
- 3) The staining solution occluded experimental tube was connected to an air-filled upstream tube and air-filled downstream tube using 1/16" nylon luers (Cole-Parmer, Vernon Hills, IL) and the technique shown in **Figure 3.7**. Both the upstream and downstream tubes were 1/16" inner diameter and 1/8" outer diameter silicone tubing (Cole-Parmer, Vernon Hills, IL) with an approximate

length of 12 inches. A stopcock was attached to the downstream end of the three connected tubes to temporarily close the tube system during transport.

- 4) The three connected tubes were then transported to the workbench.
- 5) The air-filled upstream tube was then attached to a model 1001 1mL gas-tight syringe (Hamilton Company, Reno, NV), which was secured into the acrylic syringe holder as shown in parts A and B of **Figure 3.4**. The syringe holder allowed the programmable motion of the linear motor (PS01-23x80, LinMot, Elkhorn, WI) to be directly translated to the plunger of the gas-tight syringe.
- 6) The bubble tip of the semi-infinite air bubble was advanced forward to the opening of the experimental tube by manually moving the linear motor.
- 7) The linear motor (shown in **Figure 3.2**) was then programmed by creating a comma-separated value (CSV) file corresponding to the waveform in **Figure 3.9** and loading this file into the LinMot talk r1.3.16 (LinMot, Spreitenbach, SZ) software package. It should be noted that this waveform can be programmed directly using the LinMot talk r1.3.16 interface. This waveform generates a cyclic bubble tip motion of constant velocity forward, pause, constant velocity reverse, and pause. All cyclic experiments were conducted at a fast velocity of 25mm/s.
- 8) Using the LinMot talk r1.3.16 software the linear motor was started, allowed to run for either 1 or 10 cycles, and immediately stopped. When the cycle(s) were complete, the staining solution occluded the experimental tube.
- 9) The experimental tube was disassembled from the experimental apparatus and placed in a humidified incubator for 15 mins at 37°C with 5% carbon dioxide.
- 10) The experimental tube was removed from the incubator and ready for imaging.

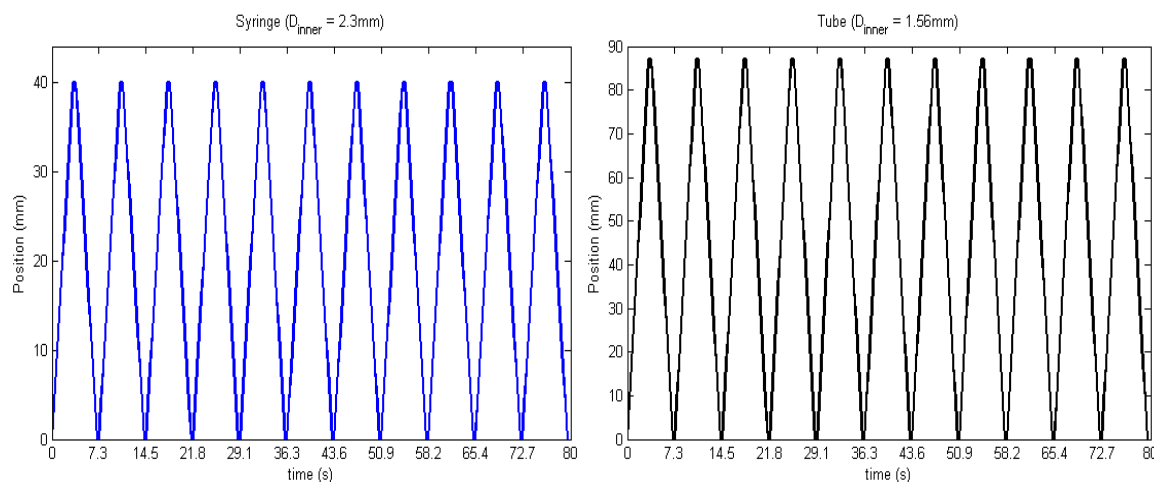


Figure 3.9: The waveform generated to run the linear motor during cyclic experiments. Left: The waveform programmed directly into the linear motor. Right: The expected waveform in the experimental tube after adjusting for the diameter change between the gas-tight syringe and the experimental tube. The result is a bubble tip velocity of 25mm/s in the experimental tube.

3.3.7. Image Acquisition

Once the conditioned cells were incubated for 15 minutes with a staining solution of Hoechst 33342 and Ethidium Homodimer-1, DPBS++ was pipetted into the experimental tubes to replace the staining solution. This dramatically reduced the light scattering and background fluorescence due to the surfactant proteins in solution. The experimental tubes were assembled into the experimental tube holder as shown in **Figure 3.3** and transported to the stage of a Nikon Eclipse TE2000-E inverted epifluorescence microscope (Melville, NY). The tube was examined using a 10x Plan Fluor objective lens with 0.30 numerical aperture (Nikon, Melville, NY).

The experimental tube was rotated so that the cell monolayer was closest to the stage and objective lens. Images were taken at fifteen positions along the bottom of each experimental tube. At each position, two images were taken to separately capture the fluorescence from the ultraviolet and green light excitations. A Nikon UV-2A ultraviolet excitation filter (Melville, NY) with 330-380nm bandpass excitation and 420nm cut-on

longpass emission (barrier) filter was used to collect the fluorescence from ultraviolet excitation of Hoechst 33342. Before rotating the filter cube to the green light excitation filter, an image was captured and stored using a microscope-mounted digital 12 bit CCD camera system (SensiCam QE, COOKE Corporation, Romulus, MI) and ImageJ with μ Manager plugin (National Institute of Health, Bethesda, MD). Subsequently, a Nikon G-2A green excitation filter (Melville, NY) with 510-560nm bandpass excitation and 590nm cut-on longpass emission (barrier) filter was used to collect the fluorescence from green excitation of Ethidium Homodimer-1. An image was again captured and stored before moving to the next position in the experimental tube. **Figure 4.2** shows example images capturing the fluorescence of Ethidium Homodimer-1 and Hoechst separately.

3.3.8. Longitudinal Cyclic Recruitment-Derecruitment Experimental

Protocol

After 22 hours of media perfusion (24 hours post-seeding with cells), the experimental tubes were removed from the perfusion apparatus. The longitudinal cyclic recruitment / derecruitment experiment is a variation on the protocol presented in the previous section. The longitudinal experiment was designed to image the same tube after 1, 5, 10, 15, and 20 cycles of recruitment and derecruitment. The longitudinal cyclic protocol follows steps 1 – 3 of the normal cyclic protocol exactly.

- 4) The experimental tube was assembled into the experimental tube holder as shown in **Figure 3.3** and transported to the microscope stage. The experimental tube holder was filled with 99.5% glycerol to provide optical coupling.
- 5) The air-filled upstream tube was then attached to a model 1001 1mL gas-tight syringe (Hamilton Company, Reno, NV), which was secured into the acrylic

syringe holder as shown in parts A and B of **Figure 3.4**. The syringe holder allowed the programmable motion of the linear motor (PS01-23x80, LinMot, Elkhorn, WI) to be directly translated to the plunger of the gas-tight syringe.

- 6) The bubble tip of the semi-infinite air bubble was advanced forward to the opening of the experimental tube by manually moving the linear motor.
- 7) The linear motor was then programmed by creating a comma-separated value (CSV) file corresponding to the waveform in **Figure 3.9** and loading this file into the LinMot talk r1.3.16 (LinMot, Spreitenbach, SZ) software package. This waveform generates a cyclic bubble tip motion of constant velocity forward, pause, constant velocity reverse, and pause. All cyclic experiments were conducted at a fast velocity of 25mm/s.
- 8) Using the LinMot talk r1.3.16 software the linear motor was started, allowed to run for one half-cycle (recruitment only), and immediately stopped. At this point the experimental tube was only filled with air, allowing for reduced scattering and background fluorescence during
- 9) Using the ImageJ with μ Manager plugin software, a multi-position acquisition was programmed for at least 6 positions along the bottom of the tube. By running the program, the microscope would move to the user-defined x,y, and z positions and take an image using the microscope-mounted digital 12 bit CCD camera.
- 10) The multi-position acquisition was run with the Nikon UV-2A ultraviolet excitation filter for Hoechst 33342. The filter cube was rotated to the Nikon G-2A green excitation filter for Ethidium Homodimer-1, and the multi-position acquisition was run again.

- 11) The linear motor was started allowed to cycle for 5 cycles, and stopped when the experimental tube was filled with staining solution.
- 12) The cells were allowed 5 mins to incubate with the staining solution at room temperature. This allowed sufficient time for the Ethidium Homodimer-1 stain to stain newly-permeabilized cells.
- 13) Steps 8 – 12 were repeated until images were acquired at all 6 positions under both ultraviolet and green excitation filters for 1, 5, 10, 15, and 20 cycles.

3.3.9. Image Analysis

The custom MATLAB (Mathworks, Natick, MA) code included in **Appendix section 7.1** was used to automatically count cells in the captured images. Automatic counting prevents the user bias and error that may arise during manual cell counting. The cell counts from images capturing Hoechst fluorescence were recorded as the total number of cells while cell counts from images capturing Ethidium Homodimer-1 fluorescence were recorded as dead cells. By dividing the dead cell population count by the total number of cells, the percent of cellular death was evaluated. In the longitudinal cyclic experiment, it was possible to track changes in total number of cells with respect to the number of recruitment / derecruitment cycles. This difference in the number of Hoechst-stained cells was reported as detached cells. For visual presentation, the Hoechst and Ethidium Homodimer-1 images were pseudo-colored and merged using ImageJ to form a single image, as shown in **Figure 4.2**.

3.3.10. Flow Cytometry Data Acquisition

To estimate the total number of cells successfully seeded into experimental tubes, flow cytometry data was collected using an Attune acoustic focusing cytometer

(ThermoFisher Scientific, Grand Island, NY). After 22 hours of media perfusion (24 hours post-seeding with cells), the experimental tubes were removed from the perfusion apparatus. The cells were collected and run through the flow cytometer according to the following protocol.

- 1) 5mL of Trypsin-0.25% EDTA (ThermoFisher Scientific, Grand Island, NY) was pipetted into the cell-seeded experimental tube. The experimental tube was placed in a humidified incubator at 37°C with 5% carbon dioxide for 10 minutes.
- 2) After cell detachment was confirmed under a microscope, the Trypsin-cell suspension was flushed out of the experimental tube and into a 1.5mL microcentrifuge tube (Celltreat, Shirley, MA) using 1mL of DPBS++.
- 3) The microcentrifuge tube was capped and placed in a MiniSpin microcentrifuge (Eppendorf, Hamburg, Germany) at 2000rpm for 2 minutes.
- 4) After centrifuging, the supernatant was removed and the cells were washed in DPBS++. The microcentrifuge tube was then placed back in the microcentrifuge at 1500rpm for 5 minutes.
- 5) After centrifuging, the supernatant was removed and the cells were resuspended in 195µL of Annexin Binding Buffer (eBioscience, San Diego, CA). 5µL of Annexin V-FITC was added to the 195µL of cell suspension.
- 6) The cells were incubated in the 2.5% Annexin V-FITC in binding buffer solution for 10 minutes at room temperature under dark conditions.
- 7) The microcentrifuge tube was then placed back in the microcentrifuge at 1500rpm for 5 minutes.
- 8) After centrifuging, the supernatant was removed and the cells were resuspended

in 190 μ L of Annexin Binding Buffer. 10 μ L of Propidium Iodide at a concentration of 20 μ g/mL was added to the 190 μ L of cell suspension.

- 9) The cell suspension was transferred to a test tube (BD, Franklin Lakes, NJ) and 300 μ L of Annexin Binding Buffer was added for a total sample volume of 500 μ L. The sample was then run through the Attune acoustic focusing cytometer for data collection.

3.3.11. Flow Cytometry Analysis

Each Flow Cytometry Standard (FCS) data file was analyzed using FlowJo 7.6.1 (FlowJo, Ashland, Oregon). FCS files were imported into FlowJo and visualized by plotting forward scatter (FSC) versus side scatter (SSC), as shown in **Figure 3.10**. FSC correlates with cell size, because large objects will refract more light than small objects. More light refracted by the object leads to more light being bent around the obscuration bar to reach the forward-positioned lens, leading to higher forward scatter signals. SSC is proportional to the granularity of the cells, meaning that cells with high internal complexity or a rough cell membrane will lead to high side scatter signals. The plot of forward scatter versus side scatter was used to gate out events with low FSC and low SSC, which were characterized as debris (**Figure 3.10**). The same gate was applied to all flow cytometry samples to prevent bias. The remaining events after gating out debris were characterized as cells and included in the total count of cells within the sample.

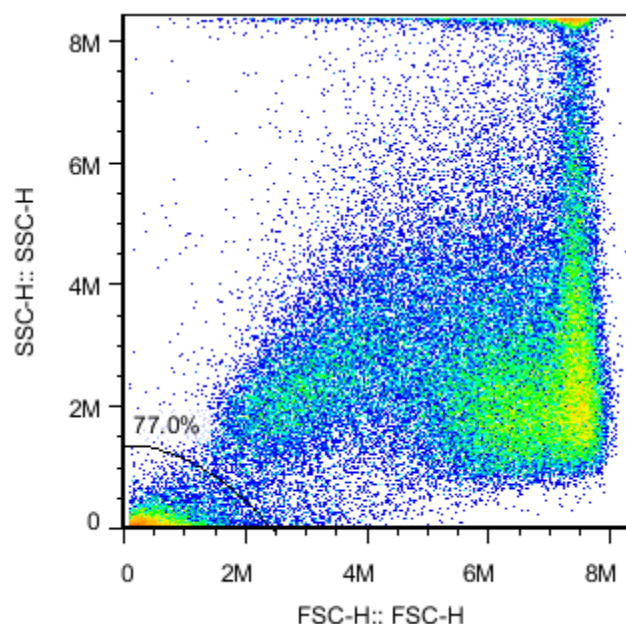


Figure 3.10: Scatter plot of the flow cytometry data from a representative sample. Forward scatter (FSC) is plotted versus side scatter (SSC), and events with both low FSC and low SSC intensities were gated out and classified as debris. The remaining events were classified as cells and reported by total count.

3.3.12. Statistical Analysis

For repeated measurements of a single variable (number of seeded cells, number of Hoechst-stained cells), the mean and standard deviation were calculated. Statistical analysis of studies involving more than two experimental groups (varied number of cycles or varied speed of recruitment) was performed using a one-way ANOVA. Specific statistical differences between each experimental group were identified using a Tukey post-hoc test. Each experimental group is represented by the mean and standard error of the mean bars.

4. RESULTS

4.1 Introduction

The goal of this study was to quantify the magnitude of cellular injury and detachment associated with interfacial stresses that arise from cyclic recruitment and derecruitment of an airway occlusion model. The ability to seed H441 epithelial cells in a high confluence monolayer within a cylindrical glass tube was evaluated using flow cytometry. When an adequate monolayer was achieved, experimental tubes were subjected to a single airway reopening event under surfactant-free conditions to generate comparable data to previous studies (Bilek *et al.*, 2003; Glindmeyer, 2013). Cyclic recruitment and derecruitment experiments were conducted in independent tubes with pulmonary surfactant for either 1 cycle or 10 cycles to demonstrate trends in cellular injury with an increase in number of interfacial flow cycles. Finally, cyclic recruitment and derecruitment experiments with pulmonary surfactant were performed on the microscope stage so that the same tube could be tracked longitudinally through 1, 5, 10, 15, and 20 cycles. This allowed for quantification of both cellular injury and cell detachment for an increasing number of cycles in a given tube. This section details the results of the described experiments for our cyclic recruitment and derecruitment model.

4.2 Flow Cytometry Cell Counting

From flow cytometry analysis of $n = 22$ tubes, it was determined that the total number of cells remaining in the experimental tubes after seeding and perfusion had a mean \pm standard deviation of $57,680 \pm 24,388$ cells, compared to about 360,000 cells

initially seeded. Sample images ($n = 32$) from the longitudinal cyclic recruitment-derecruitment experiments with a cell monolayer covering the entire field of view were analyzed and found to have a mean \pm standard deviation of 697 ± 114 cells per image. Using a stage micrometer, the image field of view was measured to be $0.09056\text{cm} \times 0.06766\text{ cm}$, corresponding to an area of 0.00613 cm^2 . Dividing the cells per image by the image area, we determined that the cell concentration from 32 images was $113,750 \pm 18,604\text{ cells/cm}^2$. We estimated that a surface area of 0.504 cm^2 was covered with cells using the following equation:

$$\text{surface area covered with cells} = \text{total \# cells} \left(\frac{\text{image area}}{\text{\# cells per image}} \right)$$

When this surface area was compared to the total lumen surface area of the tube (approximately 3.676 cm^2), we found that roughly 13.7% of the lumen surface area was covered with a high confluence monolayer of cells. This would correspond to approximately a 50° arc of the circular cross-section being covered with cells as shown in **Figure 4.1**.

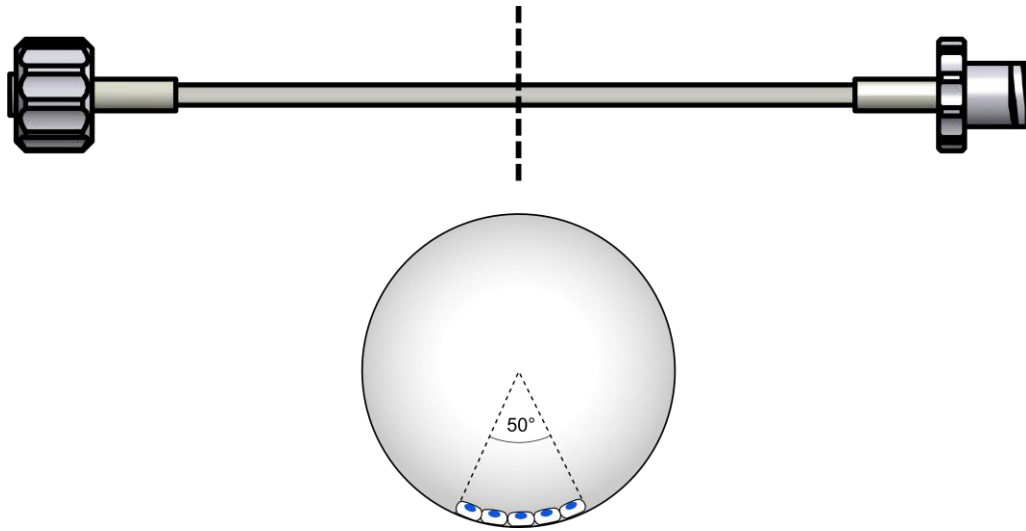


Figure 4.1: Cross section of an experimental tube showing approximate surface area covered with a high confluence monolayer.

4.3 Single Surfactant-Free Recruitment Scenario

Single recruitment events were conducted under surfactant-free conditions at a slow reopening velocity of 2.5 mm/s and a fast velocity of 25 mm/s. These two experimental groups were compared to a control group where staining solution was directly introduced without an air-liquid interface. The results of $n = 5$ trials are presented in **Figure 4.2**. The slow recruitment velocity resulted in a mean of 9.4% cell death while the fast recruitment velocity resulted in a mean of 5.7% cell death, compared to a mean of 2.1% cell death in the control group. A one-way ANOVA was conducted with Tukey post-test for significance. This statistical test indicated that the cell death measurements for slow recruitment velocity were significantly different from the control group with $p < 0.001$.

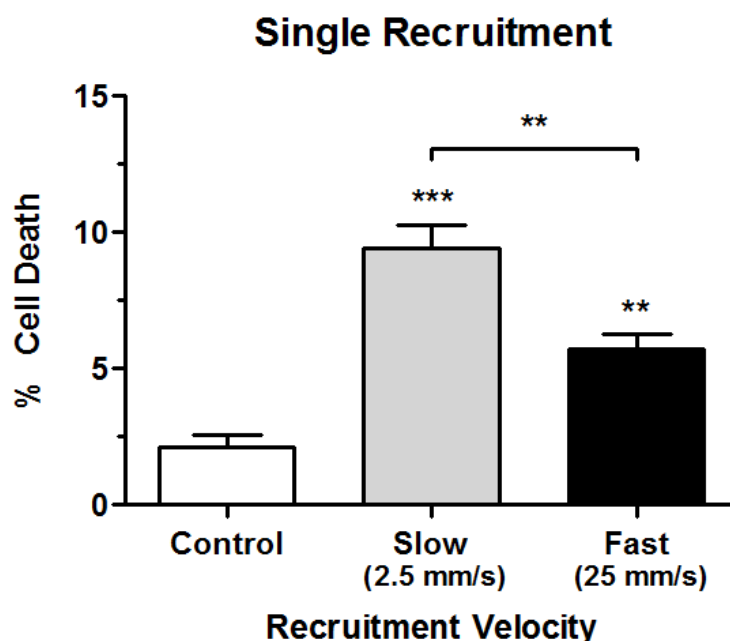


Figure 4.2: Graph comparing the percent of cell death for varying recruitment velocities for a single surfactant-free recruitment scenario. The staining solution was introduced into the recruited tube using pulmonary surfactant and a fast derecruitment velocity to minimize damage. A one-way ANOVA test was conducted for significance with a Tukey post-test (** $p < 0.01$; *** $p < 0.001$). Displayed are group means with standard error of the mean bars for $n = 5$ trials per group (control = $2.1 \pm 1.1\%$; slow = $9.4 \pm 1.9\%$; fast = $5.7 \pm 1.3\%$).

The fast recruitment velocity group was significantly different from the control group and the slow recruitment velocity group with $p < 0.01$ for both comparisons.

Representative images from a single location in experimental tubes from each group are shown in **Figure 4.3** to illustrate the visual difference that corresponds to the statistically significant numerical differences of **Figure 4.2**.

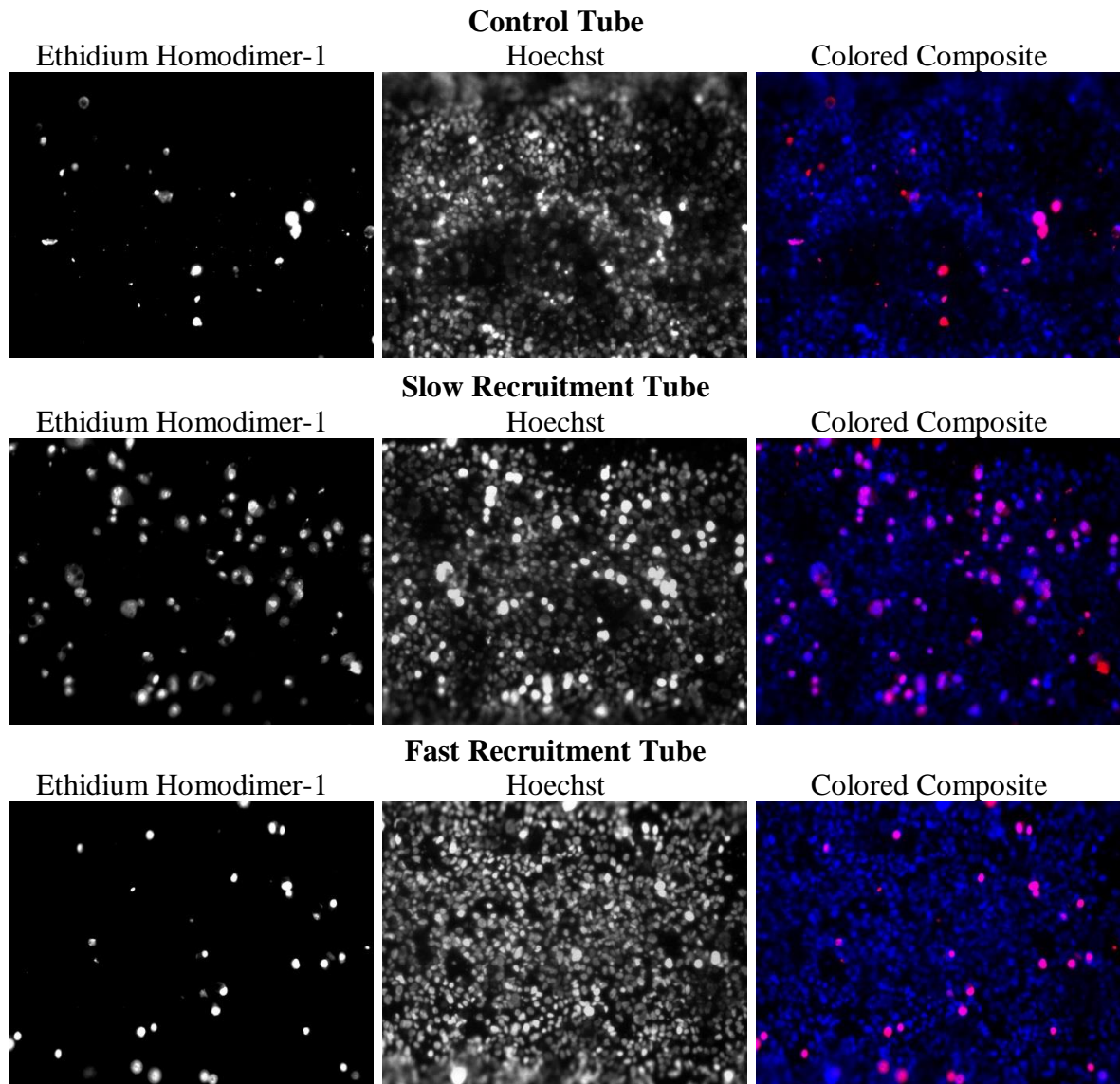


Figure 4.3: Figure showing a representative image example for each experimental group. Grayscale images were acquired separately for each stain, counted, falsely colored, and combined into a colored composite. Ethidium Homodimer-1 stains the DNA of cells with a permeabilized membrane (dead cells) while Hoechst stains the DNA of all cells.

4.4 Population Average Behavior of Cyclic Recruitment-Derecruitment

Scenario

Cyclic recruitment and derecruitment events were conducted with 1.0 mg/mL of surfactant at a fast velocity of 25 mm/s for 1 cycle and 10 cycles. These two experimental groups of $n = 5$ trials were compared to a control group of $n = 5$ trials, where the occlusion fluid was directly flushed over the cells at an average velocity of 25 mm/s, exposing the cells to equivalent flow stresses without an air-liquid interface. The results are summarized in **Figure 4.4**. One cycle of fast recruitment resulted in a mean of 4.0% cell death while ten cycles resulted in a mean of 10% cell death, compared to a mean of 1.5% cell death in the control group. A one-way ANOVA was conducted with Tukey

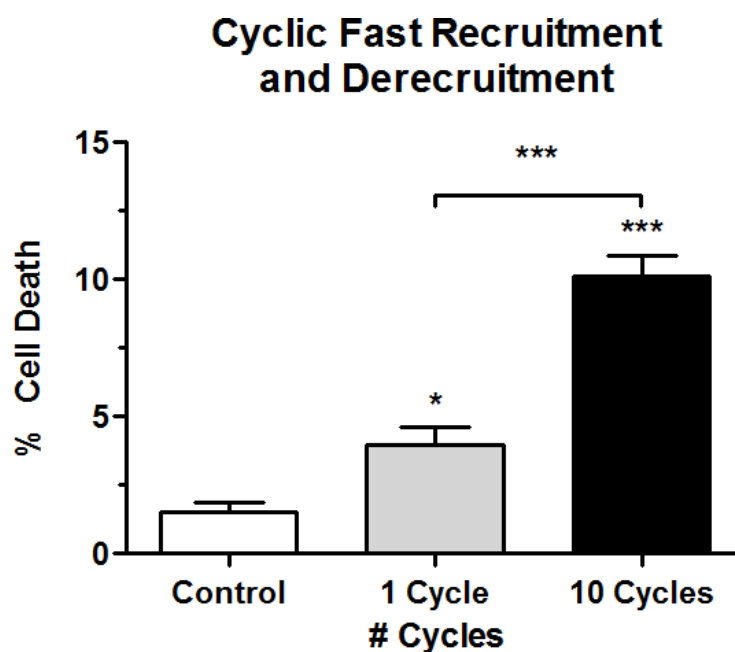


Figure 4.4: Graph comparing the percent of cell death for varying number of fast (25 mm/s) recruitment-derecruitment cycles. The staining solution with 1.0 mg/mL pulmonary surfactant was used as the occlusion fluid. The solution was displaced forward during recruitment with an air bubble and retracted back into the experimental tube during derecruitment. A one-way ANOVA test was conducted for significance with a Tukey post-test (* $p < 0.05$; *** $p < 0.001$). Displayed are group means with standard error of the mean bars for $n = 5$ trials per group (control = $1.5 \pm 0.79\%$; 1 Cycle = $4.0 \pm 1.4\%$; 10 Cycles = $10 \pm 1.7\%$).

post-test for significance. This test indicated that the cell death measurements for one cycle were significantly different from the control group with $p < 0.05$. The measurements for ten cycles were found to be significantly different from both the control group and the one recruitment cycle group with $p < 0.001$ for both comparisons.

4.5 Longitudinal Cyclic Recruitment-Derecruitment Scenario

Cyclic recruitment events were conducted with 1.0 mg/mL of surfactant at a fast velocity of 25 mm/s for 1, 5, 10, 15, and 20 cycles. Experimental tubes ($n = 5$) were imaged longitudinally. By longitudinally, we mean that the same locations within an experimental tube were imaged after sequential recruitment-derecruitment events. For example after one half-cycle (one recruitment) the tubes were imaged. To achieve 5 total cycles, we then imposed seven addition half-cycles (four derecruitments and three recruitments), allowed the stains to incubate at room temperature for 5 minutes, imposed one half-cycle (one recruitment), and imaged. Similar steps were taken to achieve 10, 15, and 20 total cycles. It should be noted that the cell injury observation lags cell detachment by one half-cycle; however, the results summarized in **Figures 4.5 and 4.6** as well as **Table 4.1** ignore this cycle aliasing.

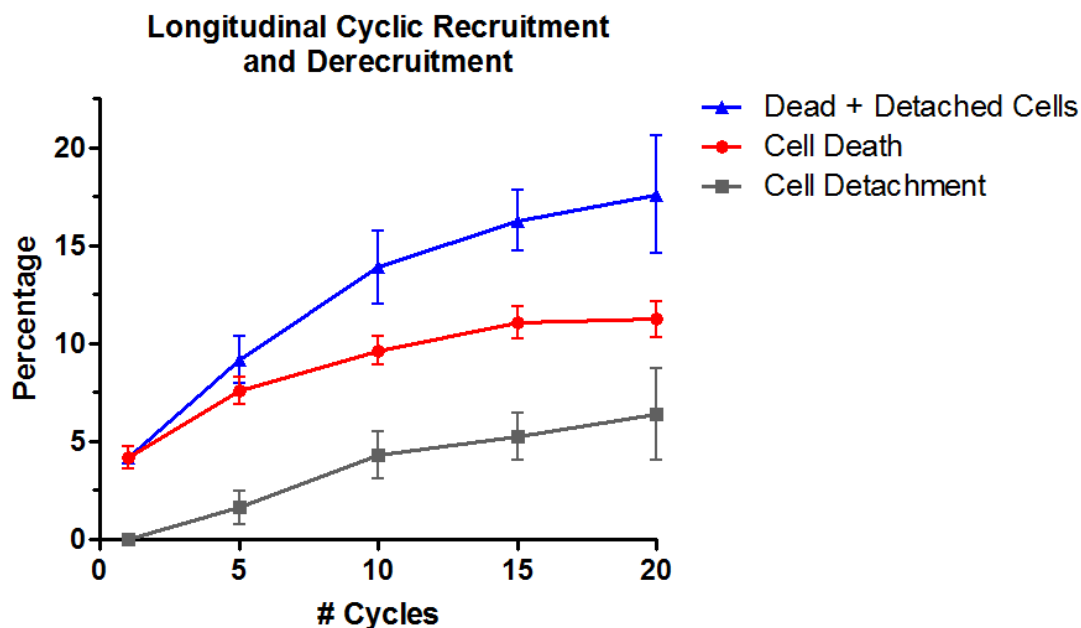


Figure 4.5: Graph of the percent of cell death, percent of cell detachment, and combined percent of cell death and detachment at 1, 5, 10, 15, and 20 cycles during the longitudinal cyclic recruitment-derecruitment scenario with $n = 5$ tubes. The staining solution with surfactant was displaced forward during recruitment with an air bubble and retracted back into the experimental tube during derecruitment at a fast velocity of 25 mm/s. Displayed are means with standard error of the mean bars.

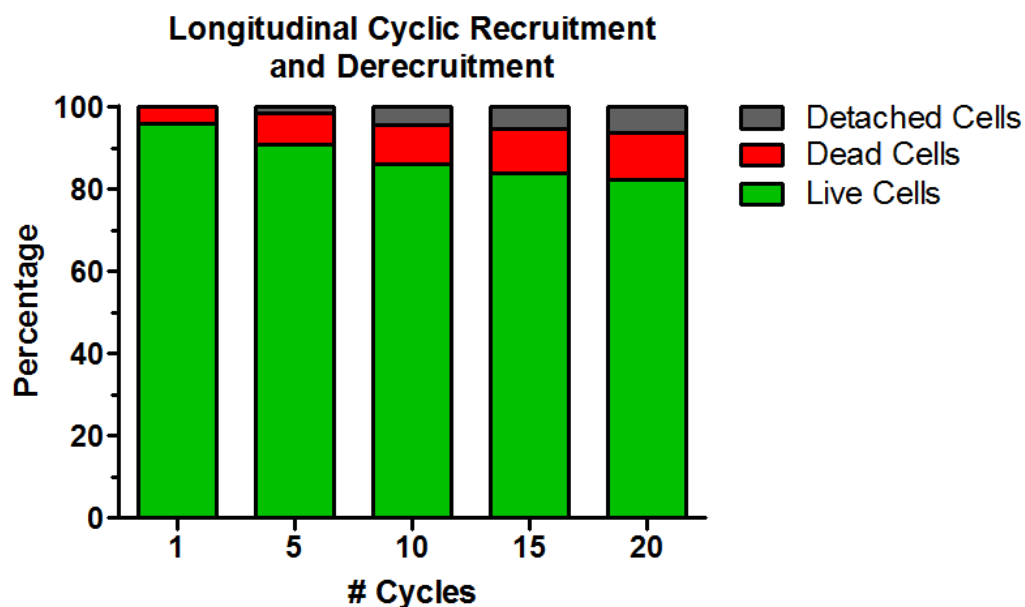


Figure 4.6: Graph of cell populations at 1, 5, 10, 15, and 20 cycles during the longitudinal cyclic recruitment-derecruitment scenario with $n = 5$ tubes. The staining solution with surfactant was displaced forward during recruitment with an air bubble and retracted back into the experimental tube during derecruitment at a fast velocity of 25 mm/s. The means of $n = 5$ tubes are displayed.

	Mean \pm Standard Deviation for All Groups				
	1 Cycle	5 Cycles	10 Cycles	15 Cycles	20 Cycles
% Dead	4.1 \pm 1.3	7.6 \pm 1.5	9.6 \pm 1.6	11.1 \pm 1.9	11.2 \pm 2.1
% Detached	0.0 \pm 0.0	1.6 \pm 1.9	4.3 \pm 2.7	5.2 \pm 2.7	6.4 \pm 5.3
% Dead + Detached	4.1 \pm 1.3	9.2 \pm 2.7	13.9 \pm 4.2	16.3 \pm 3.5	17.6 \pm 6.7
% Live	95.9 \pm 1.3	90.8 \pm 2.7	86.1 \pm 4.2	83.8 \pm 3.5	82.4 \pm 6.7

Table 4.1: Statistics for all groups of $n = 5$ trials in the longitudinal cyclic recruitment and derecruitment scenario, represented by mean \pm standard deviation.

Monolayer Delamination

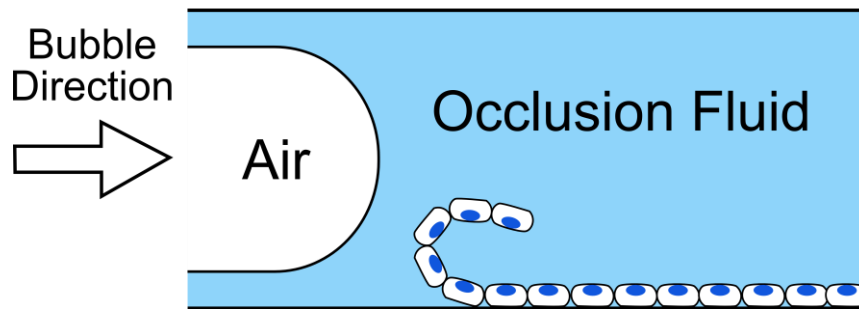


Figure 4.7: Schematic showing ‘monolayer delamination.’

4.6 Monolayer Delamination Due to Cyclic Recruitment-Derecruitment

In a separate set of cyclic experiments, delamination of the high confluence monolayer from the glass tube substrate was evident (**Figure 4.7**). These cyclic experiments followed the same protocol as the longitudinal cyclic recruitment-derecruitment scenario except that the staining solution contained only Hoechst (no Ethidium Homodimer-1 stains) and the tubes were not allowed to incubate at room temperature for five minutes between cycles. Instead the only pause between cycles was for the time it took to image the tube, estimated at 5 minutes for imaging. The behavior of the cell detachment that we observed is worth noting. In 6 out of 8 tubes the cell monolayer began to delaminate from the glass tube substrate, as shown in **Figure 4.7**. Five of the six tubes began monolayer delamination between 10 cycles and 15 cycles, with the last tube delaminating between 15 and 20 cycles. All except one tube (which was

inconclusive because all 6 observed positions were delaminated) demonstrate that the monolayer of cells delaminated from the direction of recruitment (**Figures 4.8 and 4.9**).

In no tubes did the monolayer delaminate from the direction of derecruitment.

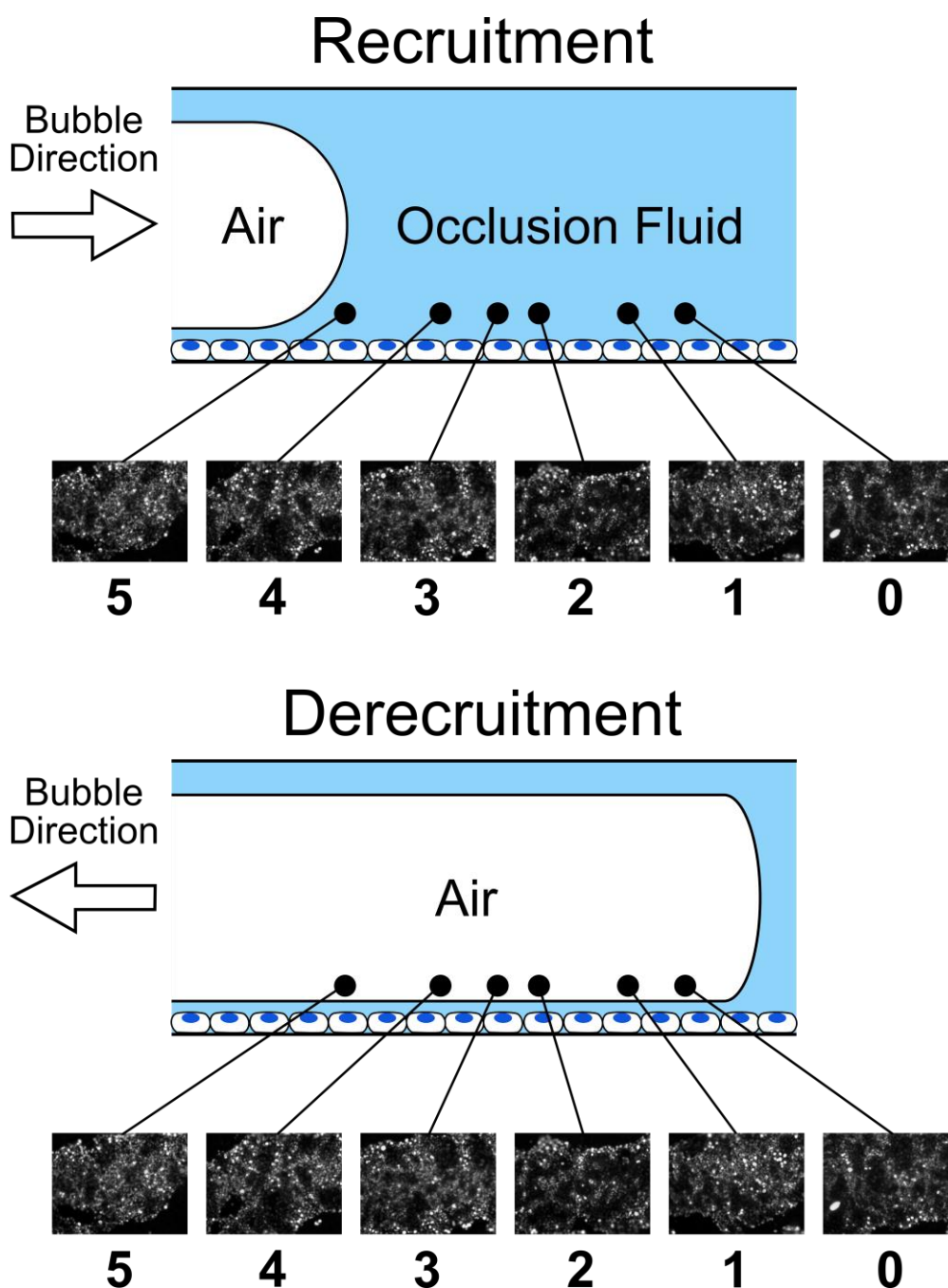


Figure 4.8: Schematic showing the directionality of recruitment and derecruitment relative to positions 0-5 used for acquiring micrographs. The exact same location was imaged after each set of recruitment-derecruitment cycles, made possible by a computerized x-y-z stage controller.

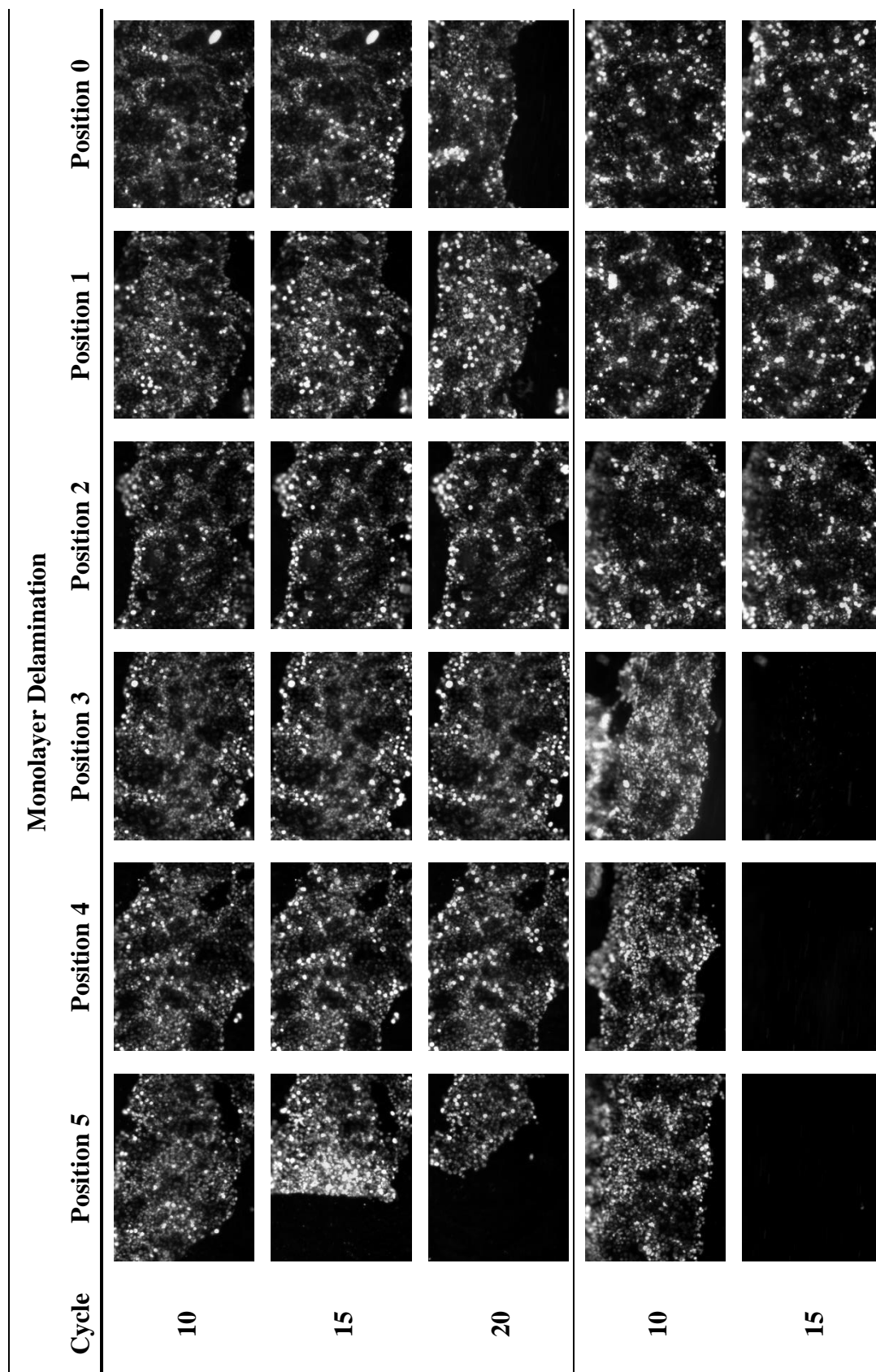


Figure 4.9: Micrographs from all 6 positions of two representative examples tubes showing ‘monolayer delamination.’

5. DISCUSSION

The monolayer delamination behavior associated with our initial cyclic experiments suggests a need to investigate modes of monolayer failure, including two possibilities described in detail in **section 5.2**. Our results indicate a lower magnitude of cellular injury compared to prior studies in both single and cyclic airway reopening. Various limitations suggest that this model could slightly underestimate cellular injury based on elapsed time for membrane repair and surfactant dysfunction. However, our results may also be slightly overestimated based on temperature and a lack of wall compliance. Overall, our model offers considerable insight into the physiologic effects of mechanical ventilation and opens several opportunities for future investigations.

5.1 Epithelial Cell Detachment with Increasing Number of Cycles

Previous *in vitro* airway reopening models have demonstrated excessive levels of cellular detachment due to cyclic recruitment and derecruitment. One goal of the current study is to track the cellular detachment in the same tube sequentially with increasing recruitment-derecruitment cycles to provide the most accurate count of cellular detachment. An alternative method would have been to count the number of cells remaining in each image and compare it to the average number of cells counted under control conditions (Yalcin *et al.*, 2007; Yalcin *et al.*, 2009). However that method would rely on achieving a control average with low variance, whereas our method of quantifying cellular detachment is specific to a given tube.

When compared to both qualitative and quantitative results from previous studies, the model produces decreased cellular detachment. Kay *et al.* qualitatively reported almost complete epithelial denudation by cycle 20 as shown in **Figure 5.1** (2004). Likewise, Yalcin *et al.* noted that at over 5 reopening events, their model produced nearly 100% detachment (2009). They also reported that 5 reopening events at room temperature resulted in $59.3 \pm 2.8\%$ detachment. Due to these high magnitudes of cell detachment, Yalcin *et al.* concluded that epithelial denudation is major implication of repeated airway reopening (2007). In contrast, we observed only about 1.6% cellular detachment after 5 cycles and 6.4% after 20 cycles. Therefore we conclude that cell denudation is not the most important mechanism of lung injury. Instead, the impacts of cellular injury by plasma membrane rupture may appear to be more prominent.

The reduction of cellular detachment in comparison to prior studies can be attributed to numerous reasons. The most significant difference between prior cyclic models and our model is our inclusion of 1.0 mg/mL pulmonary surfactant. Pulmonary surfactant both lowers and modulates surface tension during airway reopening, protecting cells from injury and detachment. Other differences include cell type, reopening velocity, and channel height. The study by Kay *et al.* used CCL-149 cells of rat origin while Yalcin *et al.* seeded cells from human cell line A549. The current study uses the H441 human cell line. The use of different cell types leads to currently unpredictable differences in cellular injury and detachment trends. We also note that Kay *et al.* used a reopening velocity of 40 mm/s with a channel height of 1.7 mm, and Yalcin *et al.* used a reopening velocity of 3 mm/s with a channel height of 0.5 mm. Our cyclic recruitment-derecruitment model uses a reopening velocity of 25 mm/s with a channel height of 1.6

mm. Pressure gradient has been established as the mechanical stress most highly correlated with cellular injury, but an association between mechanical stresses and cellular detachment has not been analyzed (Bilek *et al.*, 2003). Finally we would like to note that Yalcin *et al.* demonstrated cyclic recruitment and denuitment experiments maintained at 37°C result in significantly less cell detachment than those conducted at room temperature (2009). For this reason, our results may represent a high estimate for detachment based on a relation to temperature alone when compared to the physiologically-relevant temperature of 37°C.

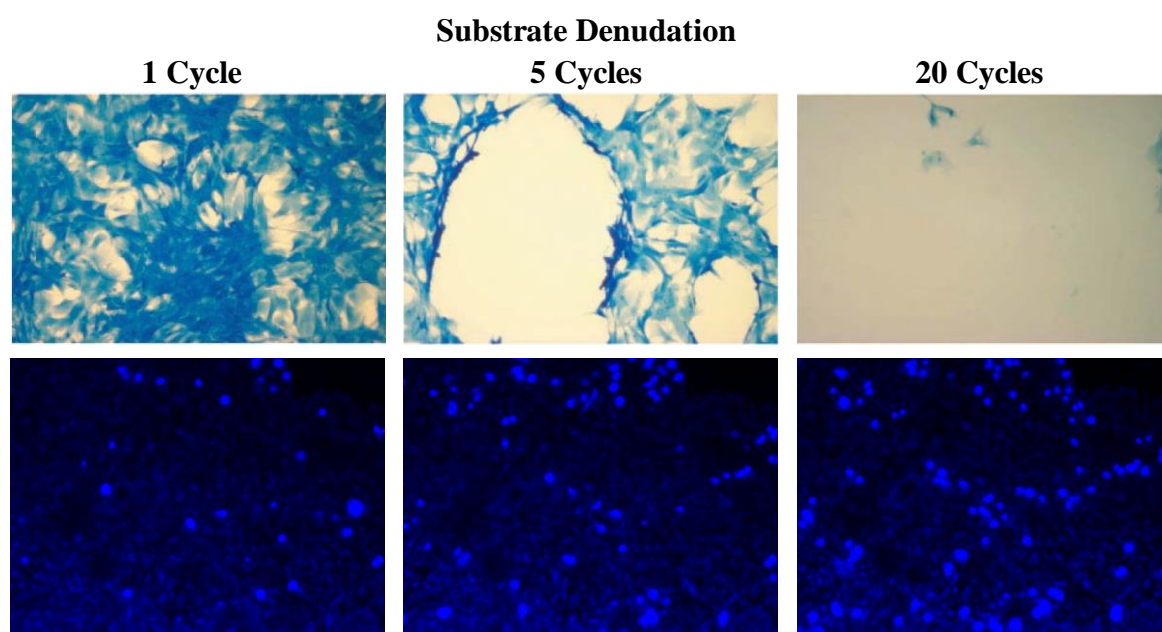


Figure 5.1: Top: Previous model by Kay *et al.* (2004). Demonstration of substrate denudation from cyclic recruitment and denuitment with L2 cells at a velocity of 40 mm/s. Cells were fixed with formaline and stained with Coomassie brilliant blue. Bottom: Current study demonstrating minimal cell detachment (about 6.4%) with H441 cells at a velocity 27 mm/s. Cells were stained with Hoechst and imaged using fluorescence microscopy.

5.2 Monolayer Delamination Behavior

We observed monolayer delamination in the direction of recruitment in five out of six tubes. No tubes displayed monolayer delamination in the direction of denuitment.

This behavior may result from a difference in mechanical stress magnitudes between air bubble progression and retraction. There are several possible modes of stress failure, but we would highlight two possibilities: 1) apical peeling due to pressure gradient, and 2) apical shear and buckling due to shear and transmitted stresses (**Figure 5.2**).

Figure 5.3 shows relevant computational results for bubble progression in the direction of recruitment (Bilek *et al.*, 2003; Jacob and Gaver, 2012). It should be noted that computational studies in rigid tube models predict an outward normal stress on the apical membrane (eliminating the apical delamination mode); however, computational studies in compliant tubes indicate the possibility of an inward normal stress (Gaver *et al.*, 1996). Jacob and Gaver found that traveling apical fluid stresses distribute through the cytoplasm toward the cell perimeter, as shown in **Figure 5.3** (2012). This stress distribution protects the cell nucleus but leaves the cell periphery susceptible to plasma membrane rupture and cell adhesion protein disruption.

It should be noted that monolayer delamination may provide a validation of the experimental model, because it indicates that the cell monolayer has reached high confluence. When seeded, H441 cells form tight junctions between neighboring cells to prevent fluid and protein passage across the pulmonary epithelial cell layer (Jacob and Gaver, 2012). Because we observed the epithelial cells delaminating as a monolayer instead of individual cells, we are confident that our model achieved a high confluence state with active tight junctions between neighboring cells.

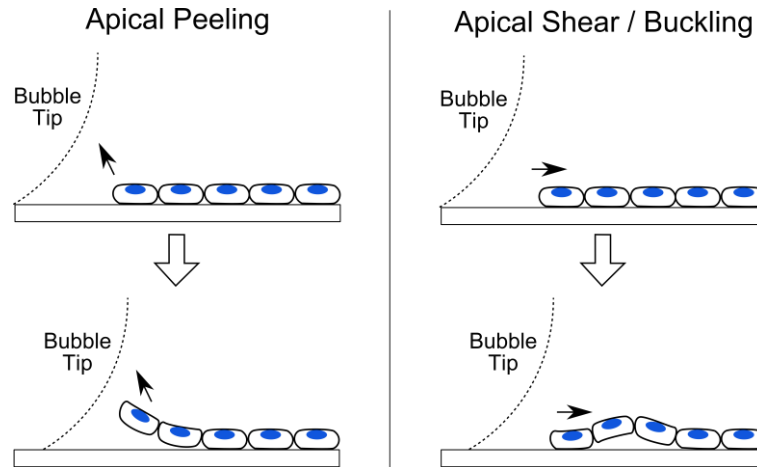


Figure 5.2: Possible modes of stress failure resulting in the observed ‘monolayer delamination,’ including apical peeling due to pressure gradient and basolateral buckling due to transmitted stresses. Once the cell layer detaches, the stress field will be modified from the ideal simulation predictions provided by previous computational models.

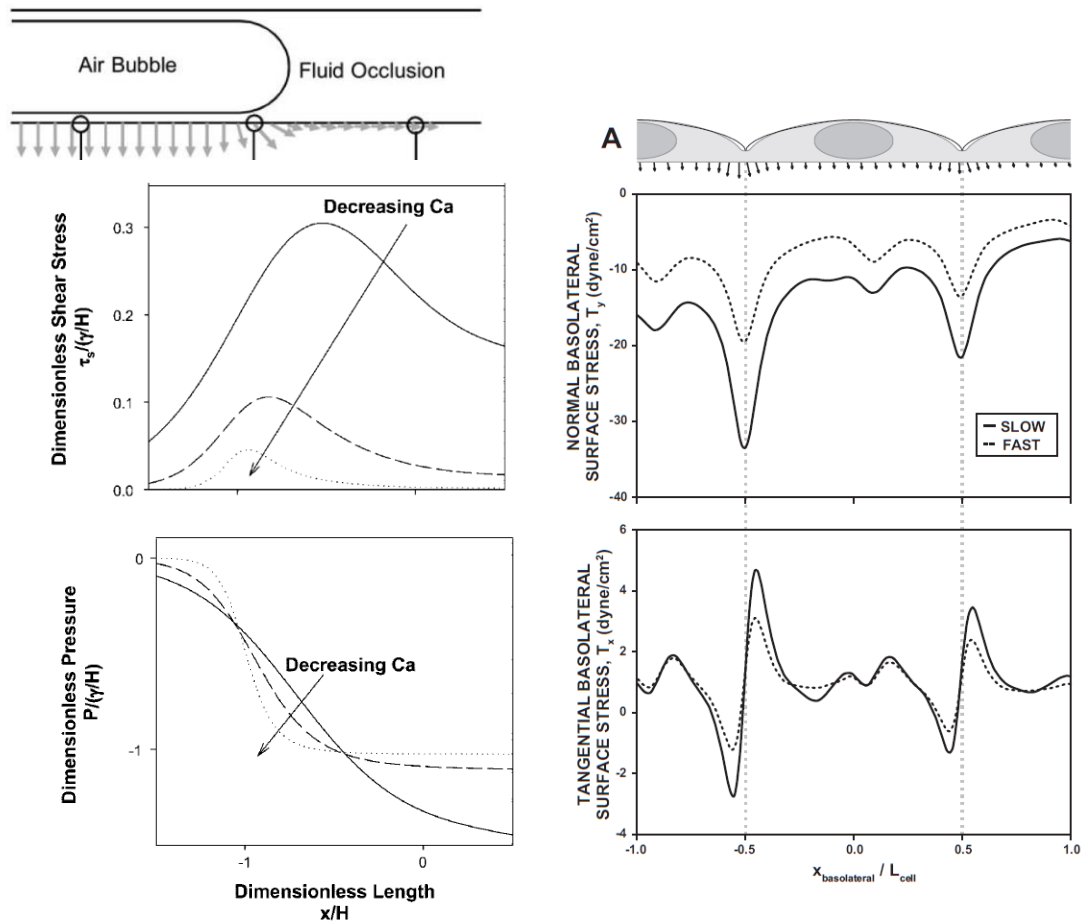


Figure 5.3: Previous computational results for mechanical stresses during airway recruitment. Left: Shear stress and pressure gradient on apical membrane (Bilek *et al.*, 2003). Right: Normal and tangential stresses transmitted to basolateral membrane (Jacob and Gaver, 2012).

5.3 Epithelial Cell Injury with Sequential Recruitment-Derecruitment Events

5.3.1. Surfactant-Free Single Reopening

The biological effect of our *in vitro* model with varying velocity was validated by passing a single semi-infinite bubble of air through the occluded airway at two different velocities. Many previous investigations have demonstrated that decreasing the velocity of reopening leads to an increase in cellular damage (**Table 2.1**). Glindmeyer provides the most comparable model with cylindrical geometry and the use of H441 cells (2013). Their results indicate that approximately 32% of cells are damaged during surfactant-free slow reopening at 2.5 mm/s while approximately 12% of cells are damaged during surfactant-free fast reopening at 25 mm/s. Our results indicate similar velocity-stimulus responses for cellular injury during slow versus fast reopening; however, we observed substantially lower magnitudes (approximately 9.4% cellular injury for slow and 5.7% for fast). Another comparable model was suggested by Bilek *et al.*, who used rat epithelial cells seeded in a parallel plate with a channel height of 1.7mm (2003). Because their reopening velocities were slightly faster (3 mm/s for slow and 30 mm/s for fast), we would expect a slight reduction in observed cellular injury. They found that the slower velocity resulted in $39.80 \pm 8.76 \cdot 10^3$ cells/cm² while the faster velocity resulted in $12.04 \pm 5.91 \cdot 10^3$ cells/cm². Our results correspond to about $14.3 \cdot 10^3$ cells/cm² injured cells for slow reopening and $7.77 \cdot 10^3$ cells/cm² injured cells for fast reopening. While the differences in the magnitude of biological response may be attributed to varying cell subculturing techniques, all three studies indicate statistically significant differences between velocity groups, indicating consistent mechanisms of damage.

5.3.2. Cyclic Recruitment and Derecruitment with Surfactant-Doped Occlusion Fluid

In this study, we initially performed cyclic recruitment and derecruitment experiments at 1 cycle and 10 cycles to confirm the trend of increasing cellular injury with increasing number of cycles. Yalcin *et al.* previously identified an increase from $21.7 \pm 1.53\%$ cell death for 1 bubble passage to $53.26 \pm 3.36\%$ for 5 bubble passages (2009). **Figure 4.4** shows the results of our study, indicating a statistically significant increase from $4.0 \pm 1.4\%$ for 1 cycle to $10 \pm 1.7\%$ for 10 cycles. While there are several physical differences between the model of Yalcin *et al.* and the current study (channel height, reopening velocity, planar versus cylindrical geometry, and surfactant) which can contribute to the difference in magnitudes, both models demonstrate an increase in cellular injury with increasing number of recruitment-derecruitment cycles.

The sequential cyclic recruitment-derecruitment experiment was performed to investigate the trend of cellular injury and detachment in the same tube with increasing number of cycles. In a prior study, Yalcin *et al.* concluded that additional recruitment events result in increased cell necrosis until a ‘critical number’ of recruitments, after which no additional cell necrosis (2007). Our experimental results do support this conclusion if cell detachment and cell death are considered separately, as shown in **Figure 5.4**. The fraction of detached cells with ruptured plasma membranes has not been quantified, but some studies assume detached cells are positive for membrane rupture and report them accordingly (Oeckler *et al.*, 2010). Because cell death appears to increase asymptotically while cell detachment increases more linearly, our data support the

concept of a ‘critical number’ of cycles but note that the inclusion of detached dead cells could confound this interpretation.

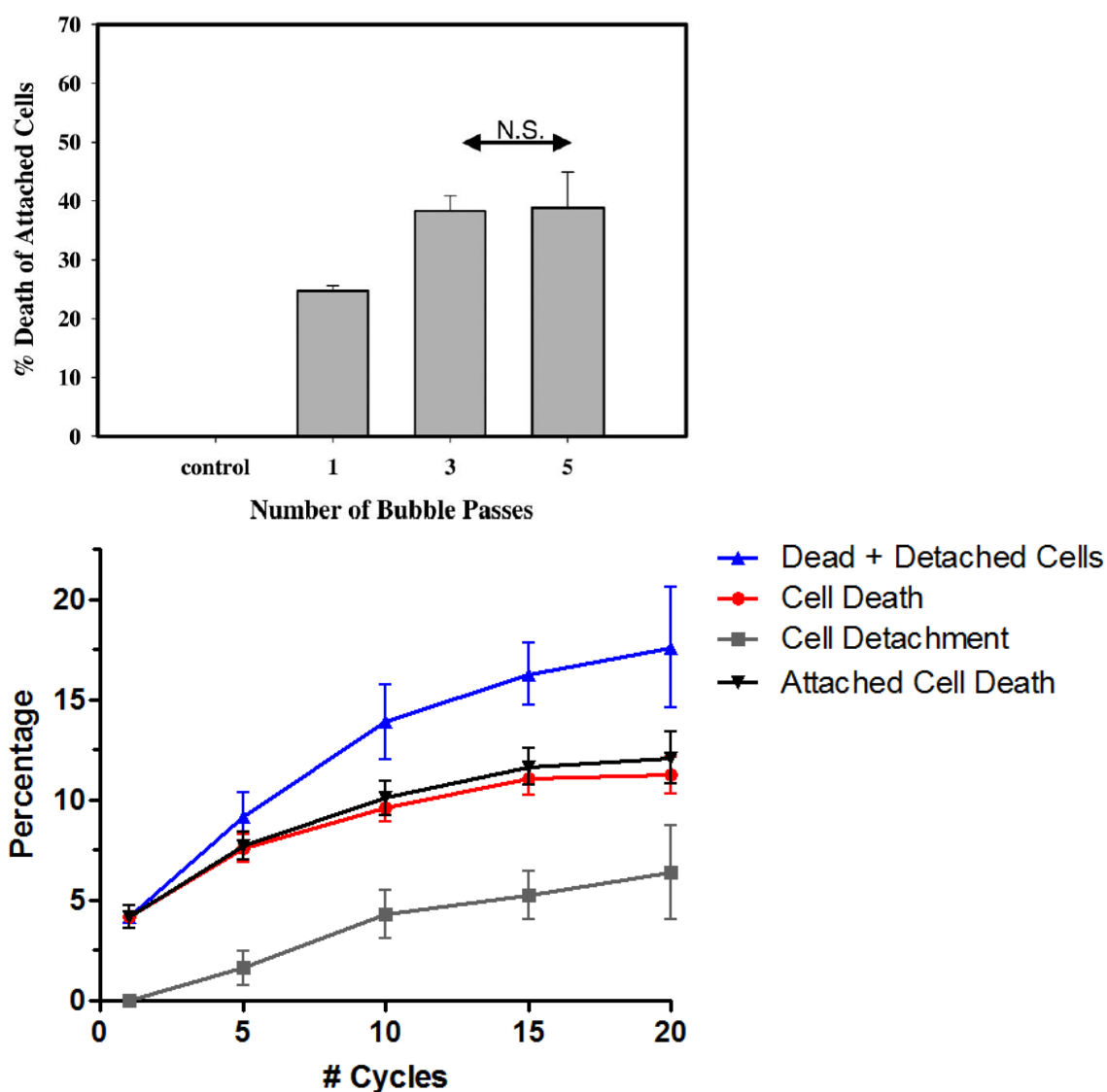


Figure 5.4: Comparison of cell death for multiple recruitment and derecruitment cycles in two models. Top: The effect of repeated bubble passes on attached cell death in an experiment by Yalcin *et al.* (2007). Note the ‘critical number’ of bubble passages is approximately 3. Bottom: The effect of repeated bubble passes on cell detachment, death, and combined death + detachment in the current study. For a more accurate comparison, the percent cell death relative to the number of attached cells was calculated and represented with a black line.

5.4 Limitations

While our study provides several insights into the cell-level response of airway reopening, there are several assumptions that limit its clinical relevance. For example after each interval of recruitment-derecruitment cycles, approximately 10 minutes elapsed prior to the initiation of the next episode of recruitment-derecruitment. This elapsed time was necessary for visualization, but could allow for membrane repair processes of wounded cells, leading to these results representing an underestimate of the true cellular injury.

The cyclic experiments of this study used an exogenous pulmonary surfactant called Infasurf. While pulmonary surfactant is important in healthy airways, surfactant can become deactivated during ARDS by interfacial competition of edema proteins. In addition, injury to type II epithelial cells can reduce the amount of surfactant produced, lowering interfacial concentrations. While 1.0 mg/mL is much less than the concentration of 35 mg/mL that is used for surfactant replacement therapy in infants, the concentration of surfactant in the liquid lining of respiratory bronchioles is unknown. If our concentration of surfactant is too high or if surfactant is deactivated in ARDS (a likely scenario), our results would underestimate true cellular injury and detachment.

All experiments presented in this study were conducted at room temperature. *In vitro* experiments by Yalcin *et al.* have demonstrated a significant difference in the magnitude of cellular injury resulting from multiple bubble passes at room temperature versus body temperature (2009). Because room temperature was shown to cause more cellular damage, our results likely reflect an overestimate of cellular injury and

detachment. To more closely mimic physiological conditions, future investigations could maintain the glycerol in the experimental holder at 37°C.

A significant limitation to this study is the use of rigid tubing. Recent studies have investigated airway reopening in flexible PDMS tubing with tube laws close to those of peripheral airways (Harrison, 2015). Not only does an increase in wall stiffness result in increased cellular necrosis and decreased detachment, but wall compliance has been shown to reverse the velocity-response trends, while maintaining stimulus-response behavior with pressure gradient (Higuera-Castro *et al.*, 2014; Harrison, 2015; Gaver *et al.*, 1996). In other words, slow velocities would result in less cellular injury than fast velocities because the pressure gradient with capillary number in flexible tubes. With this in mind, our results may be an overestimate of cell injury and an underestimate of cell detachment.

5.5 Future Work

5.5.1. Investigating Mechanisms of Monolayer Delamination

The observation of monolayer delamination from the glass substrate is an interesting result that warrants further investigation. Physiologically, this could relate to the separation of epithelial cells from the basement membrane that divides epithelial cells from endothelial cells. To determine the mechanical stress responsible for monolayer delamination, a computational approach similar to Bilek *et al.* could be used to select experimental parameters (2003). An *in vitro* model could be created where micrographs are taken from the side of a parallel plate or tubular chamber as a bubble passes over the monolayer. If the time steps of image capture were short enough, the micrographs could provide direct evidence of cell deformation under stress and which mode of failure

occurs. These results would significantly contribute to our understanding of the epithelial denudation process.

5.5.2. Cyclic Recruitment-Derecruitment in Compliant Tubing

Recent advances in the manufacturing of PDMS tubing have demonstrated the feasibility of creating flexible tubes with a tube law similar to peripheral airways (Faulman, 2015; Harrison, 2015). Compliant tubes can help to eliminate confounding results associated with a rigid substrate, as discussed in the previous limitations section. In addition, both Harrison's investigation and some of our preliminary studies not reported here demonstrate success in culturing H441 cells on PDMS. With the addition of compliant tubing, the results from cyclic recruitment and derecruitment experiments would be more representative of human physiology.

5.5.3. Cellular Conditioning for Genetic and Cytokine Tests

One promising avenue for further investigation with this cyclic recruitment and derecruitment model is the investigation of genetic and cytokine regulation associated with repeated airway reopening. The effects of cellular mechanotransduction associated with interfacial stresses are poorly understood. In addition the genetic upregulation leading to neutrophil recruitment and inflammation associated with 'biotrauma' require further investigation. We propose that our cyclic recruitment-derecruitment model can be used as a platform to condition cells and cellular fluid for genetic and cytokine testing, respectively. By analyzing the genetic regulation associated with repetitive airway reopening, fundamental knowledge can be gained about ARDS disease progression as well as links to the development of pulmonary diseases such as idiopathic pulmonary fibrosis.

5.5.4. Pulsatile Waveforms during Cyclic Recruitment and Derecruitment

Unique reopening waveforms have been shown to lower downstream cellular injury (Glindmeyer *et al.*, 2012). Pulsatile waveforms may be able to mobilize small quantities of endogenous surfactant to significantly increase concentrations at the bubble interface, thereby delivering endogenous surfactant to surfactant-depleted areas of the lung. As a bridge to animal and clinical testing, the cyclic recruitment and derecruitment model could be used to demonstrate improved endogenous surfactant function. If adopted as a mechanical ventilation technique, this could improve macroscale lung function and eventually clinical outcomes.

5.5.5. Animal Models

The models used in this study are *in vitro* experiments aimed at investigating controlled airway reopening systems with specific anatomical characteristics. The *in vitro* experiments are idealized, as discussed in the previous limitations section. The use of animal models would allow us to translate knowledge from controlled benchtop experiments to systems with complex anatomical features like airway bifurcations, mixed cell types, wall compliance, and irregular shape. Animal models can bridge the gap between human anatomy and *in vitro* models, allowing for clinical application of fundamental physical and physiological interactions.

6. CONCLUSIONS

In this study we performed cyclic airway recruitment and derecruitment *in vitro* for up to 20 cycles. This is the first demonstration of quantifying cellular injury and detachment for more than 5 cycles. By pausing between cycles, incubating the tube for 5 minutes in staining solution, and subsequently imaging the same tube we were able to track cell injury and detachment longitudinally with increasing number of cycles. With the inclusion of pulmonary surfactant and cylindrical geometry, our results indicated that the magnitude of cellular detachment is less than previously thought. We observed an average of 6.4% cellular detachment after 20 cycles with a linearly increasing trend. Prior studies found that approximately 59.3% of cells detached after only 5 bubble passes without surfactant (Yalcin *et al.*, 2009). By comparing micrographs of at the same six locations within each tube, we were able to accurately assess changes in cell injury with increasing number of cycles. We observed asymptotic behavior with cell death leveling off at about 11%. If cellular injury is considered separately from detachment, this trend confirms the conclusions of previous investigators about a ‘critical number’ of bubble passes after which no additional cell damage is induced.

Physiologically, this asymptotic trend of injury may indicate that a subpopulation of epithelial cells has a low threshold for mechanical stresses applied to their plasma membranes. Once the low-threshold cells are injured only high-threshold cells remain intact, leading to nominal change in injury with additional bubble passes. An alternative is that all cells have similar thresholds, but the cells adapt their cytoskeletal structure with

time to withstand the continued mechanical insults. It has been shown that depolymerizing actin filaments can prevent cellular injury during airway reopening (Yalcin *et al.*, 2009). Further research into these mechanisms is necessary. While our novel recruitment-derecruitment model has demonstrated basic characteristic of cyclic airway reopening, it has also provided many opportunities for further investigation in the future.

7. APPENDIX

The MATLAB (Mathworks, Natick, MA) code below was used to quantify the number of cells from micrographs. The code identifies cells by intensity differences in surrounding pixels (intensity gradients). The output of the program is the number of counted cells and a green mask over the original image to show what the program is counting.

7.1 Code

```
%Created by: Alex Itin      Adapted from: Will Glindmeyer
%This program will count the number of cells in image of your choice.
clf,clear;
%set directory to where the images are
cd('C:\Users\Alex\Desktop\Masters Research\MATLAB coding\Images to
Analyze')
%call the name of the image you wish to analyze
rgb=imread('rectangulartube_control_UV_10x_1.jpg');
%convert RGB image to grayscale
I_eq=rgb2gray(rgb);
%Find intensity peaks based on intensity difference between adjacent
%pixels. Adjust number for sensitivity.
mask_em = imextendedmax(I_eq, 30);
%creates mask overlayed on top of original image.
overlay2 = imoverlay(I_eq, mask_em, [.3 1 .3]);
%counting begins here
[L Ne]=bwlabel(double(mask_em)); %connects the dots for counting stuff
prop=regionprops(L, 'Area', 'Centroid');
total=0;
imshow(overlay2);
for n=1:size(prop,1) %counting loop based on size
    cells=prop(n).Centroid;
    X=cells(1);
    Y=cells(2);
    total=total+1;
end
hold on;
title(['Number of Cells: ',num2str(total)]); %display count in title
cd('C:\Users\Alex\Desktop\Masters Research\MATLAB coding'); %directory
%change
```

REFERENCES

- Acute Respiratory Distress Syndrome Network. "Ventilation with Lower Tidal Volumes as Compared with Traditional Tidal Volumes for Acute Lung Injury and the Acute Respiratory Distress Syndrome." *New England Journal of Medicine* 342.18 (2000): 1301-1308.
- Bernard, Gordon R. "The American-European Consensus Conference on ARDS." *Am J Respir Crit Care Med* 149 (1994): 818-824.
- Bilek, Anastacia M, *et al.* "Mechanisms of Surface-Tension-Induced Epithelial Cell Damage in a Model of Pulmonary Airway Reopening." *J Appl Physiol* 94 (2003): 770-783.
- Douville, Nicholas J, *et al.* "Combination of Fluid and Solid Mechanical Stresses Contribute to Cell Death and Detachment in a Microfluidic Alveolar Model." *Lab Chip* 11 (2011): 609-619.
- Dushianthan, A, *et al.* "Acute Respiratory Distress Syndrome and Acute Lung Injury." *Postgrad Med J* 87 (2011): 612-622.
- Faulman, Chandler J. *Investigation of Interfacial Instabilities in Compliant Airway Models*. Tulane University, 2015. Print.
- Gaver, Donald P, *et al.* "Effects of Tension and Viscosity on Airway Reopening." *J Appl Physiol* 69.1 (1990): 74-85.
- Gaver, Donald P, *et al.* "The Steady Motion of a Semi-Infinite Bubble through a Flexible-Walled Channel." *J Fluid Mech* 319 (1996): 25-65.
- Ghadiali, Samir N., and Donald P. Gaver. "Biomechanics of Liquid-Epithelium Interactions in Pulmonary Airways." *Respiratory Physiology & Neurobiology* 163 (2008): 232-243.
- Glindmeyer, Henry W, *et al.* "In Situ Enhancement of Pulmonary Surfactant Function using Temporary Flow Reversal." *J Appl Physiol* 112 (2012): 149-158.
- Glindmeyer, Henry W. *Protecting the Lung Airways through the Use of Pulsatile Reopening Waveforms*. Tulane University, 2013. Print.

- Han, SeungHye, and Rama K. Mallampalli. "The Role of Surfactant in Lung Disease and Host Defense against Pulmonary Infections." *Annals of the American Thoracic Society* 12.5 (2015): 765-774.
- Harrison, Michael C. *How Does Airway Flexibility Impact the Biological Response to Pulmonary Reopening?* Tulane University, 2015. Print.
- Higuita-Castro, Natalia, *et al.* "Influence of Airway Wall Compliance on Epithelial Cell Injury and Adhesion during Interfacial Flows." *J Appl Physiol* 117 (2014): 1231-1242.
- Huh, Dongeun, *et al.* "A Human Disease Model of Drug Toxicity-Induced Pulmonary Edema in a Lung-on-a-Chip Microdevice." *Science Translational Medecine* 159.4 (2012): 1-8.
- Huh, Dongeun, *et al.* "Acoustically Detectable Cellular-Level Lung Injury Induced by Fluid Mechanical Stresses in Microfluidic Airway Systems." *PNAS* 104.48 (2007): 18886-18891.
- Jacob, Anne-Marie, and Donald P Gaver. "Atelectrauma Disrupts Pulmonary Epithelial Barrier Integrity and Alters the Distribution of Tight Junction Proteins ZO-1 and Claudin 4." *J Appl Physiol* 113 (2012): 1377-1387.
- Kay, Sarina S, *et al.* "Pressure Gradient, Not Exposure Duration, Determines the Extent of Epithelial Cell Damage in a Model of Pulmonary Airway Reopening." *J Appl Physiol* 97 (2004): 269-276.
- Lopez-Rodriguez, Elena, and Jesús Pérez-Gil. "Structure-Function Relationships in Pulmonary Surfactant Membranes: From Biophysics to Therapy." *Biochimica et Biophysica Acta* 1838 (2014): 1568-1585.
- Mokra, Daniela, and Petra Kosutova. "Biomarkers in Acute Lung Injury." *Respiratory Physiology and Neurobiology* 209 (2015): 52-58.
- Mortelliti, Michael P, and Harold L Manning. "Acute Respiratory Distress Syndrome." *American Family Physician* 65.9 (2002): 1823-1830.
- Oeckler, Richard A, *et al.* "Determinant of Plasma Membrane Wounding by Deforming Stress." *Am J Physiol Lung Cell Mol Physiol* 299 (2010): L826-833.
- Orgeig, Sandra, *et al.* "Recent Advances in Alveolar Biology: Evolution and Function of Alveolar Proteins." *Respiratory Physiology & Neurobiology* 173S (2010): S43-S54.

- Parra, Elisa, and Jesús Pérez-Gil. "Composition, Structure and Mechanical Properties Define Performance of Pulmonary Surfactant Membranes and Films." *Chemistry and Physics of Lipids* 185 (2015): 153-175.
- Pérez-Gil, Jesús, and Timothy E. Weaver. "Pulmonary Surfactant Pathophysiology: Current Models and Open Questions." *Physiology* 25 (2010): 132-141.
- Phua, Jason., *et al.* "Has Mortality from Acute Respiratory Distress Syndrome Decreased over Time?" *American Journal of Respiratory and Critical Care Medicine* 179.3 (2009): 220-227.
- Rotta, Alexandre T, and David M Steinhorn. "Conventional Mechanical Ventilation in Pediatrics." *J Pediatr* 83 (2007): S100-S108.
- Rubenfeld, Gordon D, *et al.* "Incidence and Outcomes of Acute Lung Injury." *N Engl J Med* 353 (2005): 1685-1693.
- Salomon, Johanna J, *et al.* "The Cell Line NCI-H441 Is a Useful in Vitro Model for Transport Studies of Human Distal Lung Epithelial Barrier." *Mol Pharmaceutics* 11.3 (2014): 995-1006.
- Seah, Adrian S, *et al.* "Quantifying the Roles of Tidal Volume and PEEP in the Pathogenesis of Ventilator-Induced Lung Injury." *Annals of Biomedical Engineering* 39.5 (2011): 1505-1516.
- Slutsky, Arthur S, and Lorraine N Tremblay. "Multiple System Organ Failure: Is Mechanical Ventilation a Contributing Factor?" *Am J Respir Crit Care Med* 157 (1998): 1721-1725.
- Slutsky, Arthur S, and Marco Ranieri. "Ventilator-Induced Lung Injury." *N Engl J Med* 369.22 (2013): 2126-2136.
- Sui, Guodong, *et al.* "Solution-Phase Surface Modification in Intact Poly(dimethylsiloxane) Microfluidic Channels." *Anal Chem* 78 (2006): 5543-5551.
- Ware, Lorraine B, and Michael A Matthay. "The Acute Respiratory Distress Syndrome." *New England Journal of Medicine* 342.18 (2000): 1334-1349.
- Weibel, Ewald R. "A Retrospective of Lung Morphometry: from 1963 to Present." *Am J Physiol Lung Cell Mol Physiol* 305 (2013): L405-L408.
- Weibel, Ewald R., and Domingo M. Gomez. "Architecture of the Human Lung." *Science* 137.3530 (1962): 577-585.

Weibel, Ewald R. *Morphometry of the Human Lung*. Springer Berlin Heidelberg, 1963. Print.

Wüstneck, R., *et al.* "Interfacial Properties of Pulmonary Surfactant Layers." *Advances in Colloid and Interface Science* 117 (2005): 33-58.

Yalcin, HC, *et al.* "Influence of Airway Diameter and Cell Confluence on Epithelial Cell Injury in an In Vitro Model of Airway Reopening." *J Appl Physiol* 103 (2007): 1796-1807.

Yalcin, HC, *et al.* "Influence of Cytoskeletal Structure and Mechanics on Epithelial Cell Injury during Cyclic Airway Reopening." *Am J Physiol Lung Cell Mol Physiol* 297 (2009): L881-L891.

BIOGRAPHY

Alex Itin was raised in Franklin, TN by Robert and Joyce Itin. He graduated from Centennial High School in 2011 and is currently pursuing both a B.S.E and M.S. in biomedical engineering from Tulane University. Over the years Alex found out that he loves marine environments and working with his hands. His hobbies are kayaking, fishing, cycling, rock climbing, woodcrafting, renovating houses, and making stained glass. He is open to all of the opportunities that the world presents for future employment, but moving forward he hopes to have more spare time to enjoy both his hobbies and the company of his friends.